DEC 14 1998

SANDIA REPORT

SAND98–2607
Unlimited Release
Printed December 1998

RECEIVED
DEC 22 1998
OSTI

Molecular-Scale Lubricants for Micromachine Applications: Final Report

A. R. Burns, J. E. Houston, T. M. Mayer, T. A. Michalske, J. J. Sniegowski, S. L. Miller, M. T. Dugger, M. J. Stevens, Y. Zhou, and G. P. Lopez

Prepared by
Sandia National Laboratories
Albuquerque, New Mexico 87185 and Livermore, California 94550

Sandia is a multiprogram laboratory operated by Sandia Corporation, a Lockheed Martin Company, for the United States Department of Energy under Contract DE-AC04-94AL85000.

Approved for public release; further dissemination unlimited.

Sandia National Laboratories

Issued by Sandia National Laboratories, operated for the United States Department of Energy by Sandia Corporation.

NOTICE: This report was prepared as an account of work sponsored by an agency of the United States Government. Neither the United States Government nor any agency thereof, nor any of their employees, nor any of their contractors, subcontractors, or their employees, makes any warranty, express or implied, or assumes any legal liability or responsibility for the accuracy, completeness, or usefulness of any information, apparatus, product, or process disclosed, or represents that its use would not infringe privately owned rights. Reference herein to any specific commercial product, process, or service by trade name, trademark, manufacturer, or otherwise, does not necessarily constitute or imply its endorsement, recommendation, or favoring by the United States Government, any agency thereof, or any of their contractors or subcontractors. The views and opinions expressed herein do not necessarily state or reflect those of the United States Government, any agency thereof, or any of their contractors.

Printed in the United States of America. This report has been reproduced directly from the best available copy.

Available to DOE and DOE contractors from
Office of Scientific and Technical Information
P.O. Box 62
Oak Ridge, TN 37831

Prices available from (615) 576-8401, FTS 626-8401

Available to the public from
National Technical Information Service
U.S. Department of Commerce
5285 Port Royal Rd
Springfield, VA 22161

NTIS price codes
Printed copy: A03
Microfiche copy: A01

DISCLAIMER

Portions of this document may be illegible in electronic image products. Images are produced from the best available original document.

SAND 98-2607
Unlimited Release
Printed December 1998

Molecular-Scale Lubricants for Micromachine Applications: Final Report

A. R. Burns, J. E. Houston, T. M. Mayer and T.A. Michalske
Surface and Interface Sciences Dept.

J. J. Sniegowski and S. L. Miller
Intelligent Micromachine Dept.

M. T. Dugger
Materials Aging and Reliability: Interfaces Dept.

M. J. Stevens
Materials Simulation Science Dept.
Sandia National Laboratories
P. O. Box 5800
Albuquerque, NM 87185-1413

Y. Zhou and G. P. Lopez
Dept. of Chemical Engineering
University of New Mexico
Albuquerque, NM 87131-1341

ABSTRACT

The nature of this work was to develop the physics and chemistry base for understanding molecular-scale lubricants used to reduce of friction- and adhesion-induced failure in silicon micromachines (MEMS). We acquired this new knowledge by tailoring the molecular properties of the lubricants, applying local probes that can directly monitor the response of lubricants in contact conditions, and evaluating the performance of model lubricants MEMS devices.

Model lubricants under investigation were the silane coupling agents that form monolayer films on native oxide silicon surfaces, which is the substrate in MEMS. These molecules bind via strong surface bonds and produce a layer of hydro- or fluoro-carbon chains normal to the substrate. "Tailoring" the lubricants entails modifying the chain length, the chain chemical reactivity (H or F), and the density of chain structures. Thus much effort went into understanding the surface

chemistry of silane-silicon oxide coupling. With proximal probes such as atomic force microscopy (AFM), interfacial force microscopy (IFM), and shear force microscopy in combination with IFM, we examined the frictional and adhesive properties of the silane films with very high spatial resolution (< 100 nm) and sensitivity. MEMS structures are treated with silanes under identical conditions, and examined for friction and adhesion under operating conditions. Proper assessment of the lubricants required quantitative analysis of MEMS performance at high speeds and long operating times. Our proximal probe measurements and MEMS performance analyses form a very important link for future molecular dynamics simulations, that, in turn, should be able to predict MEMS performance under all conditions.

Table of Contents

1. The structure of alkylsilane monolayers (Stevens)

Self-assembled monolayers (SAMs) are a rich area of research and application. They are presently used as lubricants, coupling agents, coatings, and templating [1]. Since they offer a means to alter and control the chemical nature of surfaces, the number of possible applications is huge. The alkylsilanes are especially interesting because they can bond to oxide surfaces, and are thus of use to SiO_2 based microelectromechanical systems (MEMS). Because of the difficulty of probing molecular monolayers, important details of the molecular structure alkylsilane SAMs have yet to be conclusively determined. Here, results of molecular modeling show that steric repulsion determines the possible structures for various alkylsilane monolayers on silica surfaces at full coverage.

The alkylsilane SAMs are rather stable. A part of the stability has been attributed to cross-polymerization of chains by Si-O-Si bridges [2-10]. Most of the present literature on these SAMs discusses the monolayer only in the context of cross-polymerization. The covalent bonding between chains is claimed to improve the monolayer stability and explain the similar behavior for alkylsilanes on different substrates. In particular, for alkylsilanes on mica, which has no hydroxyl groups to bond to, cross-polymerization has been proposed as a possible stabilizing mechanism [11]. However, the same authors as well as others have pointed out that cross-polymerization cannot easily occur due to steric hindrances [11,12]. The length of the Si-O-Si bridge must be less than twice the Si-O bond length or 3.3 Å. In this report, it is demonstrated that packing of the headgroup limits the possible monolayer structures at full coverage. In particular, cross-polymerization *cannot* occur due to steric hindrances and density considerations for full coverage monolayers. The emphasis here is on dense, fully covered monolayers which tend to be the most technologically relevant. From a fabrication point of view, making large, defect-free monolayers requires preventing cross-polymerization.

Two specific examples of alkylsilanes are treated here. An examination of the possible packing of SAM for alkyltrichlorosilanes ($CH_3(CH_3)_nSiCl_3$) and alkylmonochlorosilanes ($CH_3(CH_2)_nSiCl(CH_3)_2$) are made and compared for n>1. It is known experimentally that the

trichloro monolayers can be formed denser than the monochloro monolayers [10]. It is shown that this is due to stronger steric hindrances in the monochloro monolayers. A key issue is the full treatment of the hydrogens. Most simulations and modeling to date have neglected the hydrogens. However, for dense monolayers the packing of the hydrogens is essential [13] as in bulk solid phases.

The basis of the present work is two simple points. First, the siloxane bridge Si-O-Si is too short to allow the aliphatic tails to be parallel without overlap of the tails (*cf.* Refs. 11 and 12). In other words, if there is a siloxane bridge between two chains, then the aliphatic tails must be splayed apart. For a dense monolayer this splay is not allowed for the tails would overlap with other chains. The second point, is that a monolayer of chains connected by Si-O-Si bridges would have twice the density that is sterically feasible and, most important, that is experimentally measured [14].

Figure 1, reminiscent of many that have appeared in the last 20 years, [2-10] shows schematically what was thought to be the cross-polymerization state. The Cl atoms on the headgroup have reacted with water on the surface to form hydroxyl groups bonded to the Si on the chain. The hydroxyl groups then react to form Si-O-Si bridges between the chains. One problem with this picture is that covalent bond lengths are much shorter than van der Waal diameters. The typical Si-O bond length is about 1.6 Å [15]. Consequently the maximum distance between Si atoms of the Si-O-Si bridge is 3.2 Å for a Si-O-Si angle of 180°. Shorter angles are more likely and yield shorter separations. The van der Waals (vdW) diameter for C is 3.5 Å and for H bonded to C is 2.5 Å [16]. The C-C separation distance in the figure matches the Si-Si distance and is 3.2 Å which is much shorter than vdW diameter implying that the C atoms overlap. The situation is actually worse. The nearest neighbor hydrogen atoms are only about 1.5 Å apart. Thus, they overlap considerably. To treat the issue properly, the complete 3-dimensional geometry must be considered.

In order to determine the packing consequences of the alkylsilane chains, a structure for the silica surface is needed. Silica surfaces are amorphous, but a crystalline structure should be

sufficient. In an amorphous structure, the range of atom-atom distances broadens in comparison to a crystal. Thus, there are stronger steric constraints in an amorphous surface than a crystalline one, and any monolayer structure forbidden on the crystal surface will be forbidden on the amorphous surface. For the silica surface, tridymite has been chosen. Quantum calculations have shown that the Si-SiO surface is well matched by a scaled tridymite SiO_2 structure [17]. Since we are particularly interested in the case of SAMs on oxidized Si wafer surfaces, this choice is appropriate. The other candidate is (111) surface of β-cristobalite. This is similar to tridymite in that the top surface layer is a hexagonal lattice of SiO_4 tetrahedrons. For both crystals, the tetrahedra alternate between pointing up and down as one moves around a given hexagon. Only the stacking sequence of the layers differs in the two crystals. Since only the top layer is relevant, the two surfaces are equivalent here.

To make the SiO_2 surface, the tridymite bulk structure is cut at Si sites bonded to the upward tetrahedra (see Fig. 2). These Si are replaced by H to provide the OH groups present on the silica surface. This gives 3 OH groups in a hexagon or 1 OH per lattice cell (Fig. 2a). The lattice constant of bulk tridymite is a=5.03 Å which gives an area per OH of 25 Å. To match the Si surface the SiO_2 lattice is compressed by 12% in the (100) direction [17] which gives 22 $Å^2$ as the area per OH. This is in agreement with the experimental value of 1 OH/20 $Å^2$ [18]. Experimentally at full coverage, the area per chain, A is in the range 22-25 $Å^2$ [14,19] and this also matches the crystal lattice. The figures in this paper show the uncompressed substrate with has A=25 $Å^2$. The uncompressed, larger area makes it easier to place the alkylsilane chains, and does not compromise the following arguments on steric hindrances.

The geometry of the crystalline surface exhibits one reason why cross-polymerization cannot occur in the monolayers. Cross-polymerization requires that each neighbor alkylsilane chain be bonded together. *All* sites of the hexagons (Fig. 2a) must then have chains above them. Thus, cross-polymerization would yield A = 11 $Å^2$ which is not possible and not observed. (Crystal alkane lattice parameters have cross-sectional area near 18 $Å^2$). It is a very important point that only *half* of the sites on a hexagon have hydroxls to bond to, for this gives the correct hydroxyl

area density. There has been confusion on this point in the literature. The determining factor for the monolayer density without cross-polymerization is the size and shape of the head group.

Ulman [3] has made some geometric arguments in favor of cross-polymerization, but, he only considers a single cluster of chains. He also claims that the C-C distance between adjacent chains can be about 4.3 Å which is easily large enough to fit the chains. Such distances are not the minimum separations for upright chains. Even from the figure in his paper, there appear to be shorter C-C separations. The discussion below exhibits the importance of a 3D treatment and shows that such separations are much tighter even without cross-polymerization. Furthermore, the separation of the hydrogen atoms are most important and they have generally been ignored.

Two alkylsilane chains have been examined: dimethylalkylmonochlorosilane (DATS) and alkyltrichlorosilane (ATS). For the purposes of determining possible structures the length of the aliphatic tail is not important so long as it is longer than 1 carbon atom. The figures show the case n=3. For both cases, one of the Cl atoms is treated as removed upon Si–O bonding via a OH on the surface. The resulting O-Si bond is put at a tilt so that the Si-O-Si angle is 141° (see Fig. 3) . This angle was chosen, because it allows all the subsequent angles in the alkylsilane chain to be their most probable and the chains are upright. This value is also well within the broad distribution of Si-O-Si angles. Experimental evidence suggests that the tilt angle of the chains is small. A nonzero tilt angle packs atoms more densely. Configurations not possible at zero tilt angle will not be possible at nonzero tilt angles. In the case of the trichloro chains the other two Cl atoms are assumed to have reacted with water to form OH groups. The other angle and bond lengths are set to there equilibrium values according to the force-field.

The value of A = 25 Å^2 is close to crystal values. Not surprisingly, attempts to have all the chain oriented identically failed due to overlap of the H atoms in adjacent chains. Consequently, herringbone configurations must be used. The 2D lattice of the akyl backbones consists of a 2 chain cell. The C-C axis is oriented at a different angle to the x-axis for the two chains. We place the chains over the OH sites of the tridymite surface with the C-C axis at angles of ±30° (Fig. 3).

This pair of angles gives the largest separations particularly for the H atoms, although as discussed below overlap still occurs for DATS.

Figure 3(a) shows 3D images of DATS. For full coverage, a DATS chain is bonded to all possible OH sites. There is not much freedom in choosing the direction of the methyl groups along the tail backbone, since the orientation of backbone H atoms limits the possible configurations. The largest separation of the methyl carbons is only 2.8 Å even for the uncompressed tridymite surface. This is much smaller than the 3.5 Å vdW radius and not physically possible. For H atoms, the situation is worse with H-H separations of 1.0 Å or less for the different configurations. The H vdW radius is 2.5 Å for H bonded to C. No fully covered configuration is possible for DATS.

Considering the dimensions and bond lengths, it is not surprising that overlap occurs. The distance between the Si to which the C are bonded and which forms part of the hexagonal lattice is 5.03 Å for the uncompressed lattice and only 4.6 Å for the compressed lattice. The distances are not much larger than vdW diameter for C. There is little space for another atom, let alone two. In comparison with ATS, there are multiple factors which together make it impossible to form a fully covered DATS monolayer. The Si-C bond length of the methyl groups is larger than the Si-O bond length of the hydroxyls. The H atoms in methyl groups are significantly larger than in hydroxyl groups. The C vdW diameter is larger than the O vdW diameter.

The above result explains why the DATS monolayers are found experimentally to be poor in comparison with ATS monolayers [10]. Saturation coverage for DATS will be less than the OH area density. Examinations of the nearest neighbors of a DATS chain show that only 2 of the 6 neighbors are allowed. Thus the area density should be about 1/3 of full coverage. Rye *et al.* [10] report that octadecyldimethylchlorosilane (ODMS) saturation coverage is about 3 times smaller than octadecyltrichlorosilane (ODTS). Below it will be shown that ODTS can achieve full coverage. These results are then consistent with experiment.

Figure 3(b) shows 3D images of ATS. As above, all the OH sites have ATS chains bonded to them. The presence of OH groups complicates the determination of the geometric constraints. The

van der Waals diameter of H depends on its environment. For a H bonded to O, the vdW diameter is 0 Å in the OPLS force-field [16] which is considerably smaller than 2.5 Å for H bonded to C. The repulsion comes from the Coulomb interaction. The radial distribution function (rdf) of alcohols give a (hydrogen bond) peak at 2.0 Å for the separation of O and H on different molecules. The rdf goes to zero at r = 1.6 Å. A complete determination of possible structures would require quantum mechanical calculations which is beyond the present work. However, even within the classical force-field, ATS can form full monolayers as is now shown.

In comparison with the DATS, the OH groups of the ATS are significantly smaller than the methyl groups. Only one H atom in the OH sidegroup also makes placing the OH groups much easier than placing the methyl groups. The hydroxyl hydrogen can be rotated about the SiO bond. By pointing the H atom downward away from the methylene groups and other OH groups the separations can be made larger. The orientation shown in Fig. 3(b) gives the H-H separations that are allowable. The shortest separation between hydroxyl hydrogens is 2.2 Å at the location labeled A in Fig. 3. The shortest separation of a hydroxyl H and a methylene H is 2.9 Å which is greater than their vdW interaction diameter, since the hydroxyl H is smaller. For DATS, the methyl C separation was too small. The shortest O-O between hydroxyls is 3.0 Å which is a bit smaller than the vdW diameter of 3.1 Å [16]. While this separation is in the repulsive region, it is thermodynamically realizable. The shortest O(H)-Si separation is 3.7 Å which is greater than the vdW separation. Likewise the O(H)-C separations are greater than the vdW interaction diameter. Thus, it is possible to have ATS with two OH pendant groups.

Given the predominance of cross-polymerization in the literature, how does one rationalize the above results with the available experimental data? First, cross-polymerization has been shown to be incompatible for a fully covered monolayer. If the monolayer is not at full coverage, then some cross-polymerization could occur. The aliphatic tails will have to be splayed and this will limit the amount of coverage. As the degree of coverage increases (beyond some 'overlap' value) the amount of cross-polymerization must decrease in order to satisfy the the packing constraints. Infrared spectroscopy is in agreement with the above predictions. Parikh *et al.* [20] have measured

IR spectra as a function of coverage. The peak at 924 cm^{-1} associated with SiO-H grows significantly with coverage. There is a broad peak at 1100 cm^{-1} associated with Si-O-Si antisymmetric stretching. The integrated intensity of this peak decreases for coverage greater than 50%. As the coverage increases the number of bridges decreases and the number of silanols increases. Since the experimental systems to date have not achieved the complete ordering assumed in the molecular modeling, there is always some cross-polymerization. To make films with full coverage over larger and larger areas requires some means to inhibit cross-polymerization.

Studies of mixed monolayers of trichlorosilanes have yielded some interested results. Fairbank *et al.* [21] claim that while mixtures of propyl- and octadecyl- trichlorosilanes cannot polymerize because of steric constraints, mixtures of methyl- and octadecyl- trichlorosilanes (C_1/C_{18}) can. The mixture C_1/C_{18} must be in a ratio 3:1 or more C_1. This claim is contradicted by our results. For full polymerization the C-C distance will match the Si-Si distance which is at most 3.2 Å and shorter than the 3.5 Å vdW diameter of C. Fairbank *et al.* used Hyperchem to perform molecular mechanics calculations. Their criteria for possible configurations appears to be whether the monolayer deforms. This is not a good criteria. It misses the fact that the vdW diameters overlap implying that the state would never occur in the first place. If one starts with a state that violates overlap constraints the repulsions in the middle of a symmetric lattice will balance out. Thus, Fairbank *et al.* see a monolayer for C_1/C_{18} which is not deformed in the middle, but is deformed at the edges. To reiterate, their calculations are not valid for concluding which structures are possible due to steric effects.

While cross-polymerization is not possible for a monolayer at full coverage, it is possible for bilayers and multilayers. In a bilayer, half of the hexagon sites have chains pointing upward and the other half have chains pointing downward. This matches the hexagonal tridymite surface composed of three tetrahedra pointing up connected by three pointing down. The upward chains bond to the upward tetrahedra and similarly for the downward chains and tetrahedra. Thus, the above arguments are not in conflict with the multilayer experimental results [22].

The IR measurements of Tripp and Hair [23-25] display no chemical bonding to the surface. Instead the monolayers are most likely hydrogen bonded to a molecular water film on the silica surface. The above arguments concerning the impossibility of cross-polymerization for fully covered monolayers remain. What would change slightly is the packing constraints since the headgroup would not have to have the same orientation in the case of ATS. The $Si(OH)_3$ group would rotate so that all the OH groups would be pointing downward to promote hydrogen bonding to the water. The constraint of the C-Si-O bond angle might effect the tilt angle of the aliphatic tail. In all, this should relieve the packing constraints a bit more in the headgroup region. In particular, the closest O-O separation would increase yielding an attractive vdW interaction instead of a repulsive one.

Recent AFM measurements on ODTS prepared using Langmuir trough techniques show a herringbone structure for monolayers with A=24 Å^2 [19]. This is consistent with the need to use a herringbone structure to satisfy the packing constraints as discussed above. The Langmuir technique may be especially well-suited for forming densely-packed monolayers over large areas by compressing the ODTS film in the Langmuir trough before cross-polymerization can occur. It would be interesting to perform IR measurements on such films to see the degree of cross-polymerization as a function of A.

In summary, cross-polymerization has been shown not to occur due to steric hindrances and density considerations for alkylsilane monolayers at full coverage. Because the siloxane bridge Si-O-Si is too short, the aliphatic tails would overlap at full coverage and a monolayer of chains connected by Si-O-Si bridges would be twice as dense as feasible and experimentally measured. Dimethylalkylmonochlorosilanes have been shown not to be able to cover a silica surface at a surface density equal to the surface hydroxyl density. On the other hand, alkyltrichlorosilanes can saturate the surface hydroxyls. The structure of the headgroup can have a profound effect on the possible structures of the monolayer. In attempting to make better, more uniform monolayers, the results of this paper should be considered. A means to prevent cross-polymerization is critical to form dense, complete coverage.

These results raise a variety of questions. The role of cross-polymerization in alkylsilane monolayers has been thought to be a stabilizer. A monolayer at complete coverage will not have cross-polymerization. Does cross-polymerization really improve the stability of these monolayers? Will such a monolayer be less stable than a monolayer at less than full coverage, but with some cross-polymerization? Self-assembled monlayers of alkanethiols on gold do not cross-polymerize, and thus should be similarly stable as fully covered alkylsilane SAMs. Is a small amount of cross-polymerization an important contribution to the stability of the monolayer? If so, does it depend where the cross-polymerization occurs, e.g. the edges, a percolating cluster? Experimentally, it is difficult to answer some of these questions, for it is necessary to measure locally the amount of the cross-polymerization found in experimental systems. It would be useful to know at the highest experimental coverages how much cross-polymerization is there? Where in the monolayer is the cross-polymerization occurring? Many other questions come to mind. This work puts a new framework upon which to think about SAMs structure, their stability and making better SAMs.

References

1. Ulman, A.*Ultrathin Organic Films: From Langmuir-Blodgett to Self-Assembly*, Academic, San Diego, 1991.
2. Sagiv, J., *J. Am. Chem. Soc.* **1980**, *102*, 92.
3. Ulman, A. *Adv. Mater.* **1990**, *2*, 573.
4. Ulman, A. *Chem. Rev.* **1996**, *96*, 1533.
5. Parikh, A. N., Allara, D., Azouz, I.B., Rondelez, F. *J. Phys. Chem.* **1994**, 98, 7577.
6. Hofmann, H., Mayer, U., Krischanitz, A. *Langmuir* **1995**, *11*, 1304.
7. Allara, D., Parikh, A.~N., Rondelez, F. *Langmuir* **1995**, *11*, 2357.
8. Ge, S., Takahara, A., Kajiyama, T. *Langmuir* **1995**, *11*, 1341.
9. Zhao, X., Kopelman, R. *J. Phys. Chem.* 1996, *100*, 11014.
10. Rye, R., Nelson, G., Dugger, M. *Langmuir* **1997**, *13*, 2965.
11. Kessel, C., Granick, S. *Langmuir* **1991**, *7*, 532.
12. Carpick, R., Salmeron, M. *Chemical Reviews* **1997**, *97*, 1163.
13. Mar, W., Klein, M. *Langmuir* **1994**, **10**, 188.
14. Tidswell, I., Ocko, B., Pershan, P., Wasserman, S., Whitesides, G., Axe, J. *Phys. Rev. B* **1990**, *41*, 1111.
15. Sarnthein, J., Pasquarello, A., Car, R. *Phys. Rev. Lett.* **1995**, *74*, 4682.

16. Jorgensen, W., Maxwell, D., Tirado-Rives, J. *J. Am. Chem. Soc.* **1996**, *118*, 11225.
17. Pasquarello, A., Hybertsen, M., Car, R. *Phys. Rev. Lett.* **1995**, *74*, 1024.
18. Zhuralev, L. T. *Langmuir* **1987**, *3*, 316.
19. Kojio, K., Ge, S., Takahara, A., Kajiyama, T. *Langmuir* **1998**, *14*, 971.
20. Parikh, A.N., Liedberg, B., Atre, S.~V., Ho, M., Allara, D. *J. Phys. Chem.* **1995**, *99*, 9996.
21. Fairbank, R., Xiang, Y., Wirth, M. *Anal. Chem.* **1995**, *67*, 3879.
22. Parikh, A.N., Schivley, M., Koo, E., Seshadri, K., Aurentz, D., Mueller, K., Allara, D. *J. Am. Chem. Soc.* **1997**, *119*, 3137.
23. Tripp, C., Hair, M. *Langmuir* **1992**, *8*, 1120.
24. Tripp, C., Hair, M. *Langmuir* **1992**, *8*, 1961.
25. Tripp, C., Hair, M. *Langmuir* **1995**, *11*, 1215.

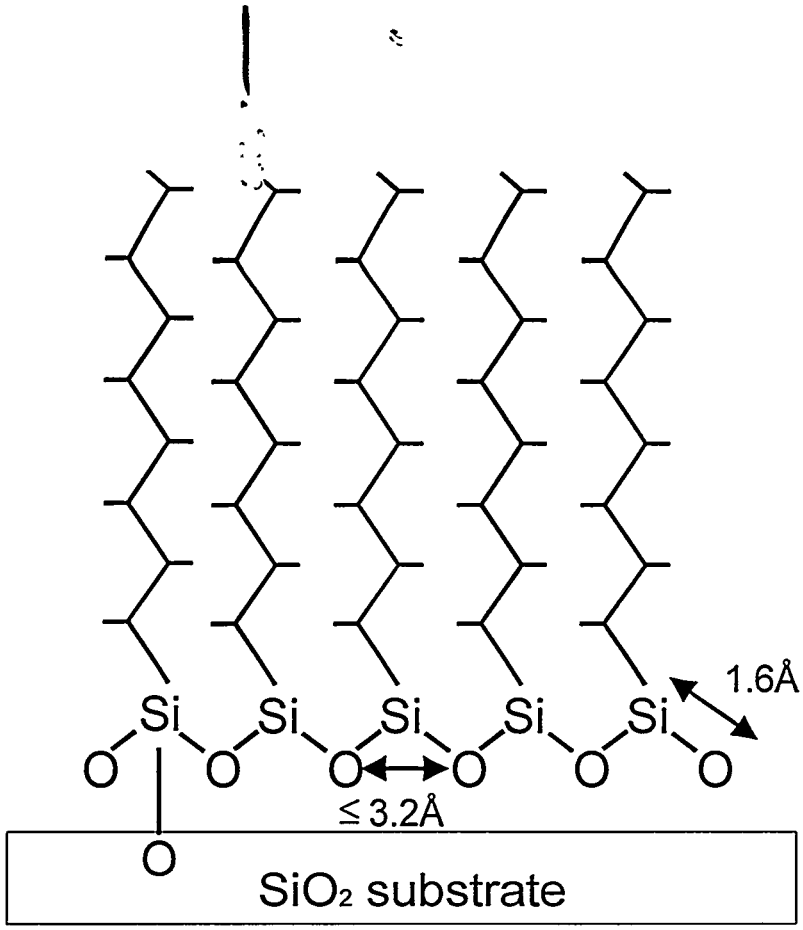

Figure 1. A typical diagram of cross-polymerization of an alkylsilane monolayer drawn to scale albeit in 2D. The alkyl chain is shown typically as a zig-zag, but with lines for the hydrogens included. The O-O distance for 180° bonds is maximal at 3.2 Å. In the figure the distance is 2.6 Å. In the planar figure, the nearest neighbor hydrogens are only 1.5 Å apart, i.e. they overlap.

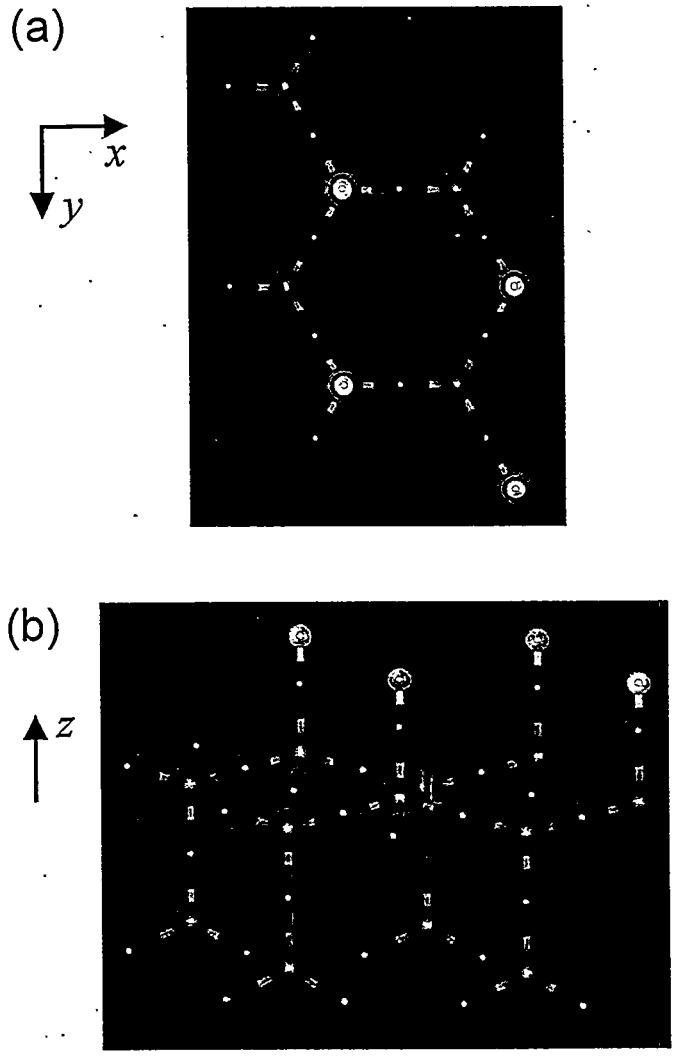

Figure 2. A 3D representation of tridymite shows 4 (2×2) cells. For this figure the lattice has not been scaled. The colorization is as follows: O is red, Si is yellow and H is white. (a) projection perpendicular to surface show hexagonal lattice. The hydroxls form a triangular sublattice. (b) a side view. The spheres have radii a fraction of the vdW radius to facilitate visibility. The straight Si-O-Si links would relax, but the hexagonal connectivity will remain for the amorphous surface.

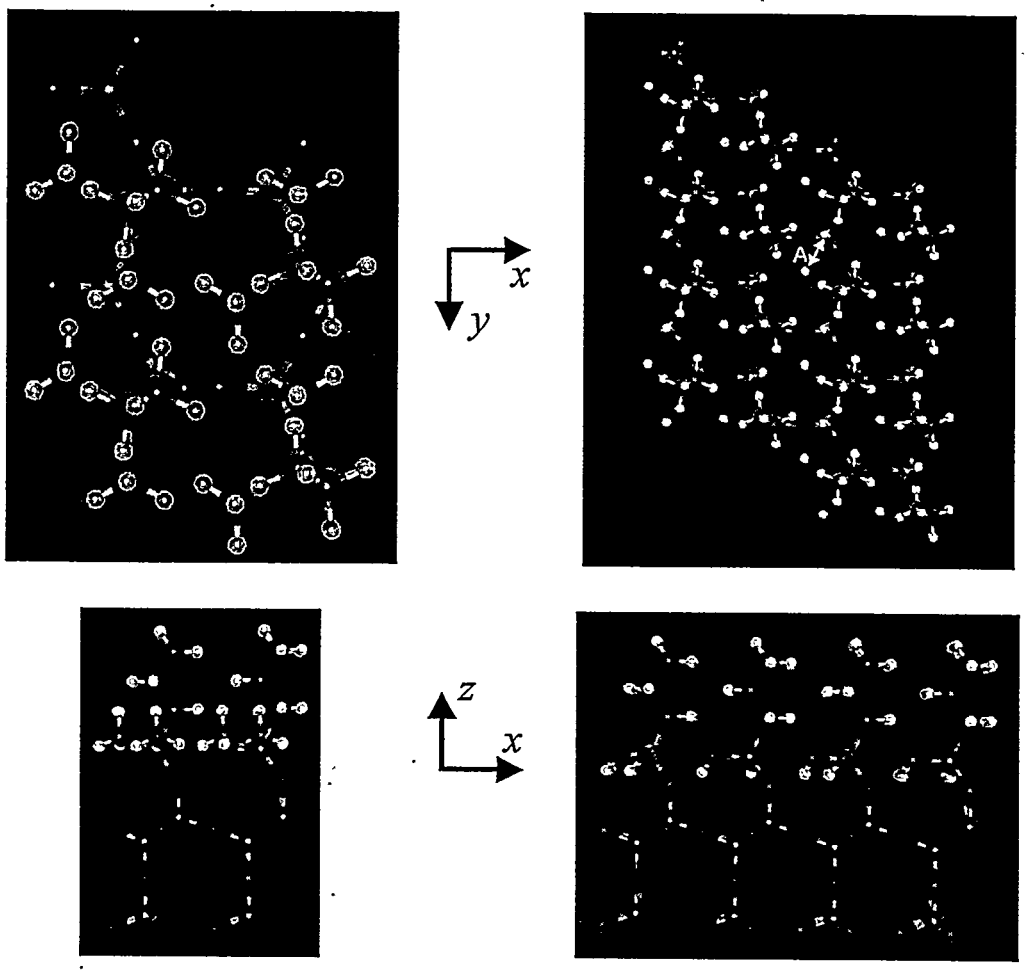

Figure 3. A 3D representation of (a) DATS chains at each silica OH site shows the short separations that yield overlaps, but (b) ATS chains do not overlap. The OH bond has been rotated 60° downward about the Si-O from a position in the *z*-plane bond. The spheres have radii a fraction of the vdW radius to facilitate visibility. Same colorization as in Fig. 2 with C atoms blue. Both the H and C atoms in the methyls groups overlap. Top part shows projection along the silica surface and bottom part projection perpendicular to the substrate surface.

2B. Interfacial Force Microscope Studies of Contact Hysteresis and Friction of Alkanethiol SAMs on Au (J.E. Houston)

The study of friction is fundamentally the study of the mechanisms by which energy is dissipated when two bodies slide past one another. These mechanisms depend upon the stress regime [1], and range from plastic deformation and fracture at very high repulsive stresses [2] to the subtle realignment of molecules as they stretch to make chemical bonds with one another at small attractive forces [3]. Within these extremes, many different mechanisms contribute to tribological properties and, if operative mechanisms can be identified and controlled, it is hoped that improvements in friction and wear behavior can be achieved.

Because of their potential as lubricants in nanoscale devices, molecularly thin organic films (liquid and solid) have received considerable attention in tribological studies (see [1],[4], [5] for reviews). One class of these films, self-assembling organic monolayers, have an added attraction in that by altering chemistry, physical properties may be changed, such that films may be tailored for specific applications [6]. As an example of this, molecular tail groups have been altered to vary adhesive energies [7],[8] and frictional properties [9-11]. In self-assembled monolayer systems, many of which are highly ordered, one characteristic that has been associated with friction is the degree of disorder [12-14]. The degree of disorder depends upon the molecule length [15], and friction forces have been inversely correlated with chain length [12-14].

The goal of this research was to identify dissipative mechanisms in a self-assembled monolayer of hexadecanethiol. It has been recognized that dissipation occurring during a cycle of contact and compression is directly related to friction [1]. We will make the same correlation among properties of monolayers when compressed between a smooth asperity and an atomically-smooth surface. In order to clearly identify dissipation mechanisms, we have used an Interfacial Force Microscope (IFM) to quantify forces and hysteretic behavior in the monolayers during a compression cycle (loading to some compressive force and then reversing). We will demonstrate that by combining nanoindentation and friction experiments, viscoelastic dissipation mechanisms can be quantified, and will show that friction in this system is dominated by contact hysteresis of the monolayer.

Additionally, we will identify several factors (film age, rate of deformation, and wear history) that influence energy dissipation.

Measurements were performed using the Interfacial Force Microscope (IFM). This instrument, which has been described in detail elsewhere [16], is distinguished by its use of a novel electrostatically-driven feedback sensor to ensure rigid displacement control during a loading experiment. Rigid displacement control ensures that instrument compliance (common in many indentation studies) does not exist, which simplifies analysis of loading cycles. In contrast to other nanoindentation instruments, there is no 'snap-to-contact' instability when using the IFM; the instrument maintains equilibrium by keeping the sensor in the same position and lowering the applied force. This characteristic of the sensor can be exploited to quantitatively map forces throughout attractive and repulsive force regimes. In addition, the IFM has the capability to perform constant-force imaging, similar to other scanning force techniques. Imaging at a low force (0.2 μN) allowed us to quantify damage resulting from our measurements.

Although the IFM was developed to measure forces while moving a probe normal to a surface, it may also be used to measure forces when sliding a probe along the surface. The force sensor maintains a balance of torques, so if the sensor and probe geometry are known, frictional forces and normal forces can be quantified simultaneously. In order to understand how this is achieved, the two feedback systems in this instrument must be identified. When a torque is developed from some applied force, it may be balanced by either activating piezos to move the base on which the sensor is mounted (constant force mode), or by applying an electrostatic force to the sensor itself (constant displacement mode). If the electrostatic force feedback were removed, the instrument would operate much like an AFM cantilever-based instrument, but adding the electrostatic force feedback provides a second method by which torques (and sensor displacement) may be controlled.

While in constant force mode, piezo extension is controlled to maintain a constant torque. If, while the probe tip is in contact with the sample, the probe is moved laterally, an additional torque develops due to a lateral friction force on the probe tip. To maintain a constant sum of all torques,

the feedback must change the normal force, which it does by increasing or reducing the depth of deformation. When moving the probe tip laterally in opposing directions, torques developed have opposing senses, which means that the depth of deformation must be increased when the probe moves in one direction and decreased when moving in the opposite direction. The result of this is a friction loop, as illustrated in Fig. 1. When moving to left (upper portion of the loop) the depth of deformation was reduced (to lower the torque due to the normal force) and when moving to the right the depth of deformation was increased. In order to quantify the friction force that results in a friction loop, the sensor and probe geometry must be known, and the change in normal force with depth of deformation must also be known.

To determine this relationship, nanoindentation loading cycles must be performed using the same experimental setup (sensor, probe, and sample). An example of a loading cycle is shown in Fig. 2, and with the experimental data, a fit to the data using Hertzian theory [17]. The Hertzian relationship is given by the expression [17],

$$F = \frac{4}{3} E^* \sqrt{R}\, \delta^{3/2} \tag{1}$$

where F is the applied force, R is the radius of curvature, δ is the depth of deformation, and E* is the composite modulus, given by

$$\frac{1}{E^*} = \frac{\left(1-\nu_{Au}^2\right)}{E_{Au}} + \frac{\left(1-\nu_{W}^2\right)}{E_{W}}, \tag{2}$$

where E_{Au}, E_W, ν_{Au}, and ν_W refer to the elastic modulus and Poisson's ratio of Au and W. Because of the good agreement with the Hertz model, we can confidently use a simple analytic expression (Eq. 1) to relate the depth of deformation to the normal force. With a known change in normal force during a friction loop, and known sample-probe geometry, we can estimate the frictional force.

The force sensor and piezo actuators were calibrated using a standard laboratory electronic balance and a displacement indicator, respectively. Both calibrations are necessary for quantitative

measurements. Probes used in this study were electrochemically etched 100 μm tungsten wires with tip radii and parabolic shape determined by field emission Scanning Electron Microscopy. Au samples with (111)-oriented facets were prepared from 99.99% pure Au wire by flame annealing [18, 19]. Immediately after preparation, samples were immersed in a 0.5 mM ethanolic hexadecanethiol ($CH_3(CH_2)_{15}SH$) solution for 24 hr to develop a self-assembled monolayer (SAM) of hexadecanethiol. Samples were dried in N_2, and were mounted for IFM interrogation, which was performed in air but under a cover to prevent exposure to light. Unless otherwise noted, the rate of displacement for force profiles was 10 Å/s and the lateral speed during a friction trace was 100 Å/s.

To investigate how the mechanical properties of the monolayer degrade over time, force profiles were acquired from new samples (0-2 days old) and from samples that had been exposed to air for 40 - 45 days. A force profile typical of new monolayer behavior is presented in Fig. 3a. Data from the loading segment of the loading cycle is marked by open circles and the unloading segment by closed circles. Force profiles from new samples showed virtually no hysteresis, indicating that little energy was dissipated during a compression cycle (loading and unloading). Fig. 3b illustrates the dependence of friction on normal force for new monolayers. Below a normal force of ~4 μN, which corresponds to a mean normal stress of 3.7 GPa, friction is minimal. The coefficient of friction was quantified by a least-squares linear fit, and in this regime it was approximately 0.004. Above 3.7 GPa it increased to 0.12. It was observed that measuring friction in this high-stress regime damaged the monolayer (a depression several Å deep was observed), so it is likely that the increase in friction is due dissipation through damage. Note that in both stress regimes, the dependence of friction on normal force was roughly linear.

The behavior of aged monolayers was markedly more hysteretic. A force profile typical of an aged monolayer is presented in Fig. 3c and demonstrates this increased hysteresis. During the loading portion of the cycle, repulsive forces were observed over a longer range than seen in new samples, and the force dropped to zero more rapidly during unloading. Note that this hysteresis is not due to an increase in adhesion (which would be observed as negative forces), but due to a

change in the spatial dependence of repulsive forces. The corresponding friction response is shown in Fig. 3d. Except for normal forces less than 1 μN, the friction force is a linear function of the applied force, with a coefficient of friction of 0.075. This is an increase in friction coefficient over that of a new monolayer of more than an order of magnitude and demonstrates that an increase of contact hysteresis produces an increase in friction.

The stresses used in this study were high (> 1 GPa), and a question that arises is whether friction forces changed with repeated measurement, i.e., does the film 'wear'? For new monolayers, force profiles and friction loops repeated in the same location remained unchanged unless stresses were above ~3 GPa. Above this threshold, a 'wear track' was observed. Aged monolayers, on the other hand, showed noticeable wear at all stresses. Fig. 4a illustrates the decrease in friction force as the same section of the sample is repeatedly probed. It decreases over the first 20-30 cycles to roughly 70 % of the initial friction force ($F_{\mu,i}$). A force profile taken after 30 cycles is shown in Fig. 4b, and when compared to that of undamaged monolayer (shown by the broken line), a reduction in the amount of hysteresis is observed. A depression approximately 10 Å deep (a 'wear track') was also observed after 30 cycles, indicating that aged monolayers can be worn by repeated deformation.

To better understand the relationship between the friction and contact hysteresis of aged films, we varied the speed at which nanoindentation and friction properties were investigated. Based on the height of the monolayer (20 Å) and tip radius, we have related the velocity during lateral (v_X) and vertical (v_Z) measurements, and found that $v_X \approx 0.08\ v_Z$. Correlations between nanoindentation and friction properties over a range of speeds are presented in Fig. 5. Fig. 5a presents F_μ/F_N as a function of v_X for aged monolayers that have not been worn (i.e., initial friction traces were analyzed). A strong speed dependence exists, with F_μ/F_N increasing with v_X. Force profiles were acquired at rates of v_Z = 5, 20 and 200 Å/s and we present loading and unloading portions of these data separately. Loading portions of these cycles are presented in Fig. 5b. At a displacement rate of 200 Å/s, the monolayer appears stiffer than it does when measured at 5 or 20 Å/s. This increase in stiffness results in greater nanoindentation hysteresis and greater friction.

Unloading portions are presented in Fig. 5c, and while there appears to be little difference between unloading at 20 and 200 Å/s, unloading at 5 Å/s results in repulsive forces over a longer range, which translate into lower hysteresis and lower friction. Nanoindentation displacement rates of 5, 20, and 200 Å/s correspond to friction measurements at 63, 250, and 2500 Å/s, which have been identified by open triangular markers on the abscissa of Fig. 5a. Thus, there is good correlation between the increase in friction and the increase in contact hysteresis with speed.

We have presented three examples of the correlation between contact hysteresis and friction, each of which demonstrate the benefit of having a versatile, mechanically stable force sensor that can quantify normal and lateral forces. We will first comment on the observation of a linear dependence of friction on normal force and then discuss the processes responsible for the age, wear, and speed dependence of friction.

We and others [10, 12, 13] have found that F_μ increases roughly linearly with F_N in the repulsive loading regime. This contrasts with measurements on other organic films [1, 20], but is likely due to the low adhesive energy of the methyl-terminated alkanethiol film [7], such that dissipation due to compressing the monolayer may be greater than that due to the adhesion-related hysteresis. Since we found virtually no adhesion for the W-alkanethiol interface (see Fig. 2-5), it is understandable that deformation losses dominate adhesion losses. In addition, our peak loads are considerably higher than those used in the earlier work.

To understand why friction forces vary linearly with normal force, we start with the assumption that the deformation of alkanethiol monolayers can be described using linear viscoelasticity [21, 22]. We approximate the monolayer with a Voigt model (spring and dashpot in parallel) and a single relaxation time constant (τ_0), such that when a constant stress rate $\dot{\sigma}$ is applied normal to the surface [23], the resulting strain becomes,.

$$\varepsilon(t) = \frac{\dot{\sigma}}{E}\left[t + \tau_o\left(1 - e^{-t/\tau_o}\right)\right]. \qquad (3)$$

Neglecting the transient response, i.e., for $t >> \tau_0$, the strain is offset below the linear elastic portion of the strain by an amount $\dot{\sigma}\tau_0/E$. Upon retracting the probe, the offset will be in the opposite direction giving rise to a hysteresis loop of strain width $2\dot{\sigma}\tau_0/E$ which varies directly with the rate of change of the applied stress. The total energy expended during the loading cycle will be given by the loop area, which is approximately given by the expression,

$$U_t = (2\dot{\sigma}\tau_0/E)\sigma_0 = 2(\sigma_0\tau_0/t_0)^2/E, \quad (4)$$

since $=\sigma_0 = \dot{\sigma}t_0$. Again, we see that the energy expended per loading cycle varies with the stress rate. If we're moving a probe, the total energy will be that of Eq. (4) times the volume of material deformed. In the case of the thiol SAM, of course, the maximum deformation h is limited by the film thickness and is measured to be about 10-15 Å, judging from the extent of the loop in Fig. 5b. Thus, since the Au substrate can be further deformed after the film is fully compressed under the center of the probe, the volume of compressed film will vary as the contact area times h.

If, on the other hand, a constant normal stress σ_0 is applied to a probe while it is moved laterally at a speed v_x, the overall effect will be to move the strained volume at the lateral rate. This volume motion cost nothing in terms of elastic deformation energy. However, the viscous loss will appear the same as if a volume of material equal to 2ahd has been deformed. Thus, a motion through a lateral distance d will result in an expended energy given approximated by Eq. (4) with

$$U = 2(\sigma_0\tau_0/t_0)^2/E \bullet 2ahd. \quad (5)$$

The rate at which energy is expended will then be Eq. (5) divided by the time required to make the lateral displacement, i.e., multiplied by the lateral velocity. That is,

$$dU/dt = = 2(\sigma_0\tau_0/t_0)^2/E \bullet 2ahv_x. \quad (6)$$

Since $dU/dt = dU/dx \bullet dx/dt = F_\mu v_x$, we finally have,

$$F_\mu = 4(\sigma_0\tau_0/t_0)^2/E \bullet ah. \quad (7)$$

If we further assume that the Au deformation is Hertzian so that a varies as $F_N^{1/3}$ and Eq. (7) implies that F_μ varies directly as F_N. The $(\tau_0/t_0)^2$ term in Eq. (7) embodies the viscous nature of the deformation and shows that the frictional force should vary as the square of the lateral deformation rate.

It is worthwhile to point out how different sample configurations give rise to different scaling behavior between friction and normal forces. From the above, we expect friction forces to be linearly dependent on the normal force when a thin layer is investigated with a spherical probe. If the layer were not thin, the volume that dissipates energy would scale as a^3, and we'd expect $F_\mu \propto F_N^{4/3}$ [2, 17]. Alternatively, if a flat, cylindrical punch were used to characterize a thin layer, a would be independent of F_N, and we'd expect $F_\mu \propto F_N^{2/3}$. Thus, the functional dependence of F_μ on F_N is specific to the experimental arrangement.

We can alternatively consider friction in terms of an interfacial shear strength,

$$\tau_\mu = \frac{F_\mu}{\pi a^2} \propto F_N^{1/3}. \tag{8}$$

Since the applied stress, also scales as $F_N^{1/3}$, we observe that $\tau_\mu \propto \sigma$, which is consistent with the general description of τ_μ [2]:

$$\tau_\mu = \tau_0 + \mu\sigma. \tag{9}$$

This description of the interfacial shear strength is very general and has been applied to friction when plastic deformation of metals is involved [2], in the very high stress regime (the 'cobblestone' model) [1], and for Langmuir-Blodgett monolayer films on mica [25]. A pressure-dependent interface shear strength has been observed in systems of thin organic films [4], and has been observed for alkanethiol monolayers via atomistic simulations [26].

Using the above framework, we can rationalize our observed speed dependence of friction. We have assumed a single relaxation time constant, even though it is known that viscoelastic behavior is typically described by a relaxation spectrum [27]. The relaxation spectrum of the

monolayer is a signature of the molecular relaxation mechanisms occurring [27, 28]. For alkanethiol monolayers, important mechanisms are changes in tilt angle of molecular chains [26]. It is believed that loading cycles produce a cycle in tilt angle, and that the characteristic time constant of the tilt restoring force directly relates to the observed hysteresis. Although the simplicity of our single-relaxation approach precludes a complete description of loss mechanisms in these films, it does give some insight into our observations.

We can approximate the loading cycle of our experiment as a linear increase in stress to a peak stress of $\hat{\sigma}$ over some time t, followed by a decrease to zero stress at the same rate. Thus, $\dot{\sigma} = \hat{\sigma}/t$. This time is related to the lateral velocity of the tip and the contact radius through the relation $t = a / v_x$, giving $\dot{\sigma} = \hat{\sigma} v_x / a$. If we substitue these two relationships for $\dot{\sigma}$ and t in Eq. 5, we obtain

$$\mathcal{U} = \frac{\hat{\sigma}^2}{E}\left(\frac{v_x \tau_o}{a}\right)^2\left[1-\left(1+\frac{a}{v_x\tau_o}\right)e^{-\left(\frac{a}{v_x\tau_o}\right)}\right]. \qquad (10)$$

One of the relaxation time constants for aged hexadecanethiol films has been reported to be 0.08 s [21], and for the contact radii of this investigation (100-300 Å), the maximum loss occurs well beyond our accessible speed range, which may explain why we observe no peak in friction. However, this simple model does illustrate the general increase in friction with speed that we observe.

Although time constants are best measured by instantaneously imposing a stress or strain and monitoring the relaxation, we can draw some conclusions about relaxations in the film by performing loading cycles at various speeds. During loading (Fig. 5b), there appears to be a relaxation rate between 20 and 200 Å/s. Force-deformation relationships are nearly identical for 5 and 20 Å/s, but increasing the displacement rate to 200 Å/s results in higher forces for equivalent deformations. A relaxation rate of between 20 and 200 Å/s translates to a time constant of between 0.1 and 1 s. However, there appears to be a separate time constant for retraction. In Fig. 5c, retracting the tip at 20 or 200 Å/s results in stresses dropping to zero within the first several Å of

movement. When retracting the tip at 5 Å/s, the monolayer can at least partially relax, which is observed by a repulsive force that decreases to zero over approximately 15 Å. Thus, relaxation occurs at a rate somewhere between 5 and 20 Å/s, giving a time constant of between 1 and 4 s. These longer time constants indicate that multiple relaxation rates do exist in aged films and that friction is speed dependent even at the lower limits of scanning capabilities.

Details of monolayer deformation have been investigated via both experimentation [21] and atomistic simulation [26, 29], which provide the basis for an understanding of how aging increases contact hysteresis. Unstressed self-assembled hexadecanethiol monolayers have a tilt angle from the surface normal (θ) of roughly 30° [6, 15, 29]. Molecular dynamics simulations of uniform compression of this system indicates that compression involves three structural changes [26]: the tilt angle of the molecules increases to a maximum of 48°, bonds within the chains are elastically compressed, and a structural transition whereby some of the sulfur head groups shift from three-fold hollow to two-fold bridge sites, occurs. These changes were all found to be reversible, and, in a study of the tribological properties of this system, the primary dissipation mechanism was oscillation of the tilt angle of the alkyl chains, resulting in a friction coefficient of < 0.02 for two contacting monolayers [26]. Our results on the friction coefficient and the amount of hysteresis in new monolayers are consistent with these predictions, and we take the view that changes in friction and hysteresis are due to changes in the freedom of movement of alkyl chains.

It has been established that lower packing density is associated with higher friction [13]. Interchain interactions dominate the energetics of monolayer compression [29], so that with high packing density, alkyl chains move in concert [29]. With low packing density, the movement of each chain is less dependent upon that of its neighbors, so that compression of the film can involve less concerted movement of chains. Compression of a less ordered film involves non-uniform changes in tilt angle and the formation of gauche defects [30]. Since vibrational chain movement is the dominant mechanism of dissipation [26] and less ordering increases freedom of chain movement, if reduced packing density occurs during aging, we expect higher friction.

The aging of hexadecanethiols in air has been associated with ozonolysis [31]. An increase in θ [32], fragmentation of the alkyl chain [33], and the oxidation of thiolate species to sulfonate species [34] have been observed during aging. It is also believed that aging involves an increase in disorder [35]. The causes of disordering may be the incorporation of oxygen into the adsorbed sulfur layer or the reduction in interchain interactions resulting from chain fragmentation, but regardless of which mechanism leads to disorder or lower packing density, it is clear that the changes taking place result in greater friction and hysteresis.

We also observed strong wear behavior. Scanning repeatedly reduced contact hysteresis and friction and resulted in a depression in the film. There appeared to be transient and steady-state components to both the contact hysteresis and friction in that hysteresis and friction decreased over the first 30 cycles, but persisted after many more. Additionally, we observed the cessation of the transient component to coincide with attaining the limit of film damage (10 Å). With a reduced film thickness, we attribute the reduction in friction during wear to a reduction in the volume of material that can dissipate mechanical energy. An alternate possibility is that wearing the film also involves a reordering once the thickness has been reduced. It is important to point out, however, that 1) friction after wearing the film is still much greater than in new monolayers and 2) even after repeated wear at high stresses the film still passivates the probe-sample interaction.

We consider two damage mechanisms: the removal of a fraction of the monolayer and the fragmentation of alkyl chains. Regarding the first, sulfonates bind more weakly to Au than thiolates [36, 37] such that one method of patterning films is through oxidation and rinsing in an alcohol [37]. It is likely that the compressive stress applied by the probe (> 1 GPa) is sufficient to displace and remove sulfonates. In this case, wearing the film would involve removal of a certain fraction of sulfonate species and the attached alkyl chains. Fragmentation of alkyl chains is reported to be aided by the oxidation process [33] and the act of measuring friction may remove the fragmented species. The high stresses may also fragment additional chains. Both mechanisms would give rise to the observed behavior, and with either the loss of a fraction of sulfonates or

fragmentation of alkyl chains, we expect a reduction in the volume available to dissipate mechanical energy and a corresponding reduction in friction.

We have developed a technique that permits the direct comparison of friction and mechanical properties on the nanometer scale. We have applied this technique to investigate the sources of friction in self-assembled monolayers of hexadecanethiols and have observed a strong correlation between contact hysteresis and friction. In all monolayers, friction forces increased linearly with applied normal force, allowing us to characterize friction using a coefficient. Contact hysteresis and friction were observed to increase with age, and we propose that aging of the film results in a reduction in packing density when stressed, which leads to greater chain mobility and more modes of energy dissipation. Additionally, we have identified that aged films wear rapidly at high stresses and have identified the dependence of friction on rate of deformation.

References

1. Israelachvili, J.N., *CRC Handbook of Micro/Nano Tribology*, in *CRC Handbook of Micro/Nano Tribology*, B. Bhushan, Editor. 1995, CRC Press: Boca Raton. p. 267.

2. Bowden, F.P. and Tabor, D., *The Friction and Lubrication of Solids: Part II*. 1964, Oxford: Clarendon Press.

3. Burns, A.R., Houston, J.E., Carpick, R. and Michalske, T.E., Phys. Rev. Lett. (1998).

4. Carpick, R.W. and Salmeron, M., Chem. Rev. **97**, 1163-1194 (1997).

5. Colton, R.J., Langmuir **12**, 4574-4582 (1996).

6. Ulman, A., Chem. Rev. **96**, 1533-1554 (1996).

7. Thomas, R.C., Houston, J.E., Crooks, R.M., Kim, T. and Michalske, T.A., J. Am. Chem. Soc. **117**, 3830 (1995).

8. Ulman, A., Evans, S.D., Shnidman, Y., Sharma, R., Eilers, J.E. and Chang, J.C., J. Am. Chem. Soc. **113**, 1499 (1991).

9. Noy, A., Frisbie, C.D., Rozsnyai, L.F., Wrighton, M.S. and Lieber, C.M., J. Am. Chem. Soc. **117**, 7943-7951 (1995).

10. Kim, H.I., Koini, T., Lee, T.R. and Perry, S.S., Langmuir **13**, 7192 (1997).

11. Tsukruk, V.V., Everson, M.P., Lander, L.M. and Brittain, W.J., Langmuir **12**, 3905-3911 (1996).

12. Lio, A., Charych, D.H. and Salmeron, M., J. Phys. Chem. B **101**, 3800-3805 (1997).

13. McDermott, M.T., Green, J.-B.D. and Porter, M.D., Langmuir **13**, 2504-2510 (1997).

14. Xiao, X., Hu, J., Charych, D.H. and Salmeron, M., Langmuir **12**, 235-237 (1996).

15. Porter, M.D., Bright, T.B., Allara, D.L. and Chidsey, C.E.D., J. Am. Chem. Soc. **109**, 3559-3568 (1987).

16. Joyce, S.A. and Houston, J.E., Review of Scientific Instruments **62**, 710-715 (1991).

17. Johnson, K.L., *Contact Mechanics*. 1996, Cambridge: Cambridge University Press.

18. Hsu, T. and Cowley, J.M., Ultramicroscopy **11**, 239 (1983).

19. Schneir, J., Sonnenfeld, R., Marti, O., Hansma, P.K., Demuth, J.E. and Hamers, R.J., J. Appl. Phys. **63**, 717-721 (1988).

20. Carpick, R.W., Agraït, N., Ogletree, D.F. and Salmeron, M., J. Vac. Sci. Technol. B **14**, 1289-1295 (1996).

21. Joyce, S.A., Thomas, R.C., Houston, J.E., Michalske, T.A. and Crooks, R.M., Physical Review Letters **68**, 2790-2793 (1992).

22. Salmeron, M., Neubauer, G., Folch, A., Tomitori, M., Ogletree, D.F. and Sautet, P., Langmuir **9**, 3600-3611 (1993).

23. Williams, J.G., *Stress Analysis of Polymers*. 2nd ed. 1980, Chichester: Ellis Horwood Limited.

24. Persson, B.N.J., *Sliding Friction*. p. 79, 1998, Berlin: Springer.

25. Briscoe, B.J. and Evans, D.C., Proc. Roy. Soc. London **A380**, 389-407 (1982).

26. Tupper, K.J. and Brenner, D.W., Thin Solid Films **253**, 185-189 (1994).

27. Ferry, J.D., *Viscoelastic Properties of Polymers*. 1980, New York: John Wiley & Sons.

28. McCrum, N.G., Read, B.E. and Williams, G., *Anelastic and Dielectric Effects in Polymeric Solids*. 1991, New York: Dover Publications.

29. Tupper, K.J. and Brenner, D.W., Langmuir **10**, 2335-2338 (1994).

30. Tupper, K.J., Colton, R.J. and Brenner, D.W., Langmuir **10**, 2041-2043 (1994).

31. Zhang, Y., Terrill, R.H., Tanzer, T.A. and Bohn, P.W., J. Am. Chem. Soc. **120**, 2654-2655 (1998).

32. Horn, A.B., Russell, D.A., Shorthouse, L.J. and Simpson, T.R.E., J. Chem. Soc., Faraday Trans. **92**, 4759-4762 (1996).

33. Norrod, K.L. and Rowlen, K.L., J. Am. Chem. Soc. **120**, 2656-2657 (1998).

34. Hutt, D.A. and Leggett, G.J., J. Phys. Chem. **100**, 6657 -6662 (1996).

35. Dishner, M.H., Feher, F.J. and Hemminger, J.C., Chem. Comm. , 1971-192 (1996).

36. Tarlov, M.J. and Newman, J.G., Langmuir **8**, 1398-1405 (1992).

37. Tarlov, M.J., Burgess, D.R.F., Jr. and Gillen, G., J. Am. Chem. Soc. **115**, 5305-5306 (1993).

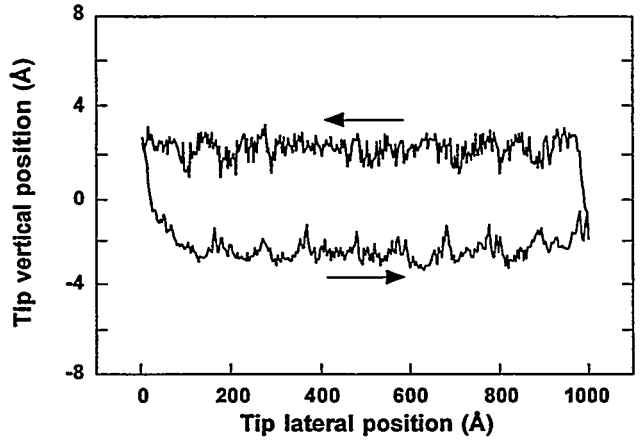

Fig. 1 Typical friction loop from an IFM friction experiment. Friction forces give rise to additional torques on the sensor, for which the feedback compensates by increasing or reducing the torque due the normal force (i.e. changing the depth of deformation). Moving to the left, feedback retracted the tip from the sample and moving to the right, it increased the depth of deformation.

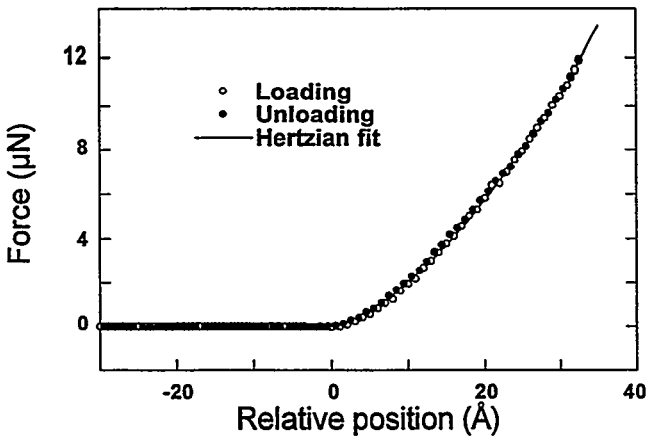

Fig. 2 Loading cycle demonstrating near-elastic behavior of monolayer-Au couple. Data shows a very good fit to the Hertzian model, which is used to estimate the change in normal force with change in tip vertical position.

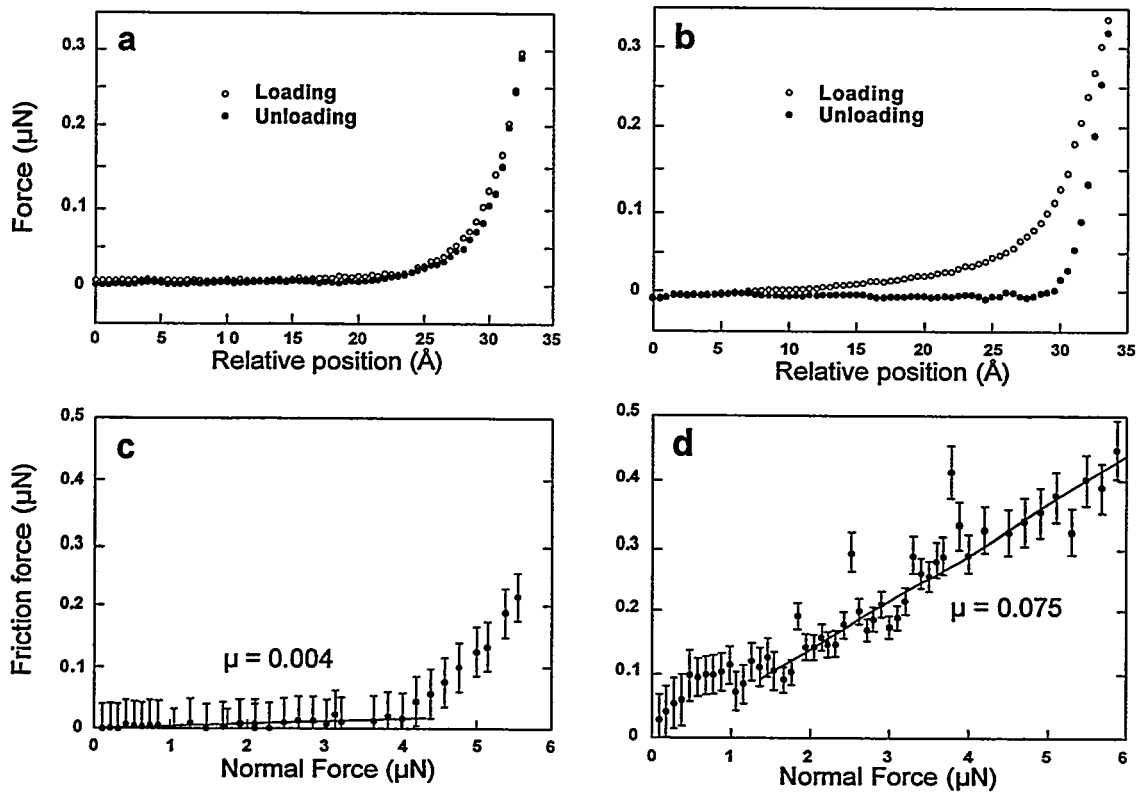

Fig. 3 Correlation between contact hysteresis and friction. (a) Loading cycle demonstrating the minimal contact hysteresis of a monolayer 0-2 days old. (b) Loading cycle of a film that was exposed to air for 40 days. A distinct increase in hysteresis is observed in the aged monolayer. (c) Friction force as a function of normal force for a new monolayer. Friction is minimal. (d) Friction vs. normal force for the aged monolayer. Friction forces rise linearly with normal force at a much greater rate than for new monolayers.

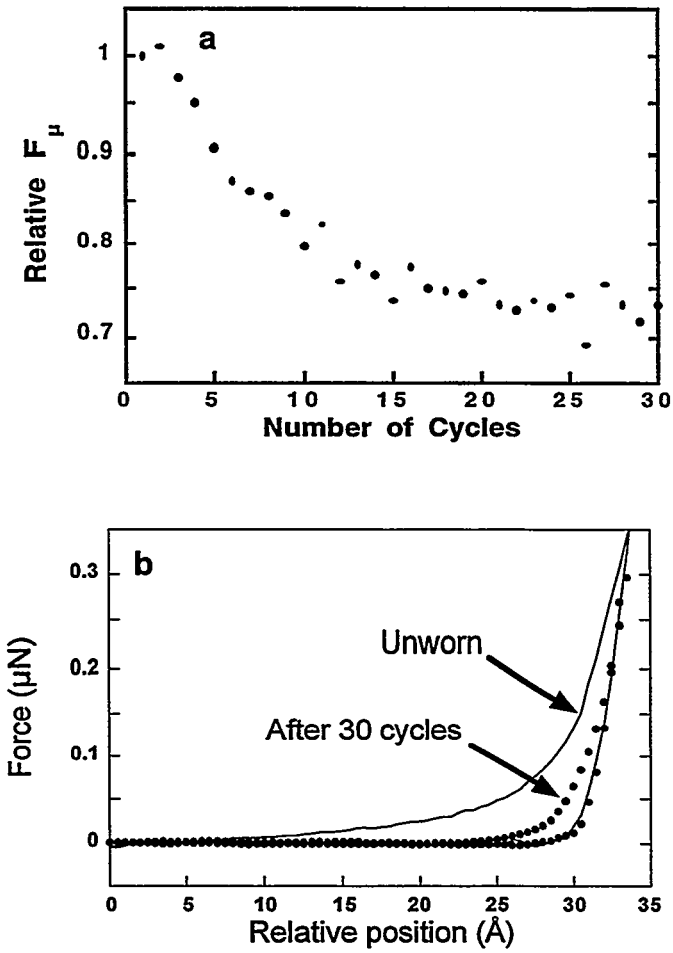

Fig. 4 (a) Normalized friction coefficient as a function of number of measurement cycles in the same location for aged films. The friction force (F_μ) is normalized by that of the first measurement cycle ($F_{\mu,i}$). Friction forces drop to ~ 75% of their original value over 20 - 30 cycles. (b) The change in contact hysteresis with wear. The behavior of the monolayer after thirty wear cycles is shown, and, for comparison, behavior of an unworn, aged monolayer is shown by the broken line. The reduction in contact hysteresis with wear correlates with the reduction in friction.

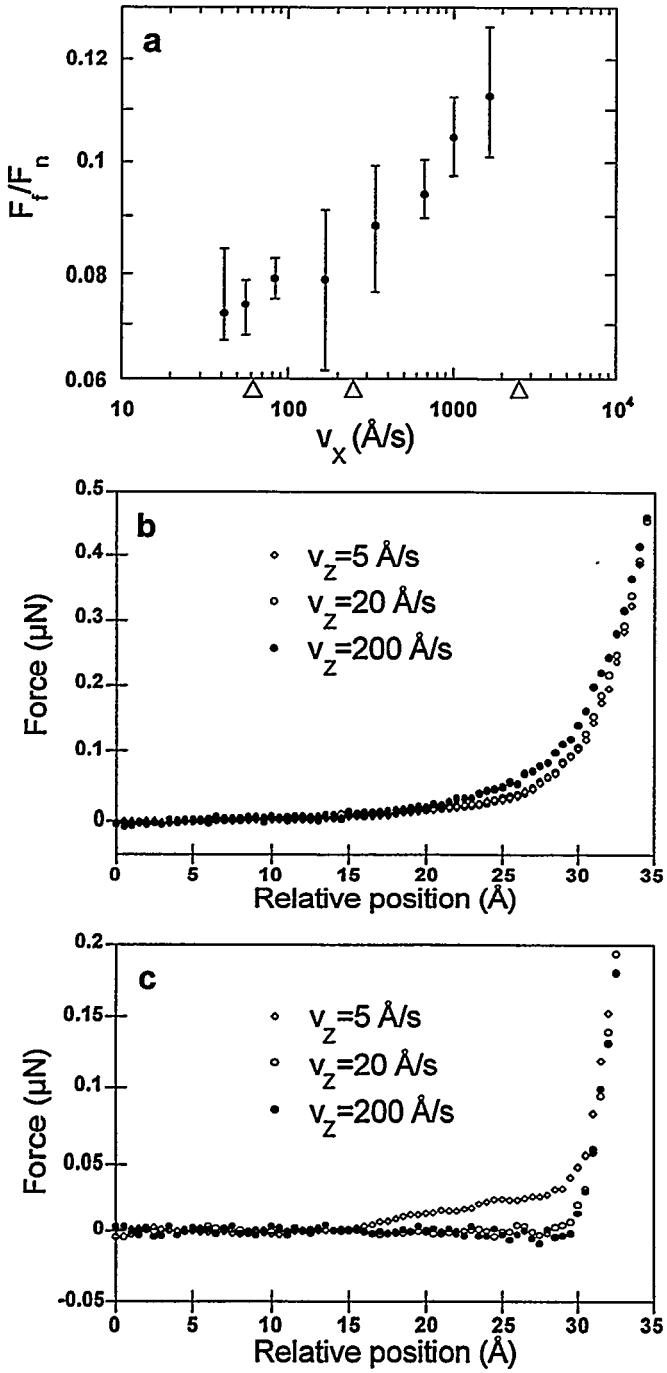

Fig. 5 (a) Dependence of normalized friction force on lateral tip speed (v_x), quantifying the increase in friction with deformation rate. The open arrows along the abscissa identify the lateral velocities (62.5, 250, and 2500 Å/s) that roughly correspond to v_z = 5, 20 and 200 Å/s. (b) Loading portion of loading cycles at three speeds. Force-deformation relationships appear to be the same for deformation rates of 5 and 20 Å/s, but the film appears stiffer at 200 Å/s. (c) Unloading portion of loading cycles at three speeds. At 5 Å/s, recovery of the monolayer is observed, while at 20 and 200 Å/s, virtually no relaxation is observed.

2B. Molecular Level Friction as Revealed with IFM/Shear Force Microscopy (Burns, Houston, and Michalske)

Our understanding of friction has advanced considerably in recent years by fundamental studies, both experimentally and computationally, at the molecular level [1-3]. Energy dissipation mechanisms include vibrational and electronic losses to the substrate [1], as well as interfacial bonding forces [2, 4]. Recently, there has been substantial work on the effects of "model lubricants" on interfacial friction. In particular, self-assembling alkanethiols [5] and silanes [6] have been used extensively because they can be tailored to examine "mechanical" parameters such as chain length, packing density [3, 7], and cross-linking [8], as well as "chemical" parameters such as adhesive molecular bond strengths [9, 10]. Mechanical and chemical effects can be difficult to separate for the chain-like silanes and alkanethiols because they are anchored firmly, relative to more fluid lubricants, to substrates by their head groups.

The effects of model lubricants on the relationship between friction and load have been studied with the surface forces apparatus (SFA) [4, 11] and the scanning probe atomic force microscope (AFM) [3, 9, 10]. Both the spring-based SFA and cantilever-based AFM exhibit mechanical instabilities when making ("jump to contact") and breaking ("pull off") interfacial contacts in the common situation where the attractive force gradient exceeds the respective spring constants. Thus the exact relation between friction, interfacial bonding, and load is obscured since friction forces are generally measured only in the repulsive regime of the contact, or for a limited range preceding pull-off that has both repulsive and attractive components [12]. This situation is exacerbated when chemical modification of the free tail groups leads to stronger adhesive forces at the interface and hence much greater force gradients [9, 10]. Finally, the finite mechanical coupling between the normal and lateral force sensing modes of a typical AFM cantilever [13] must also be taken into account in examining the friction-load relation of model lubricants.

In this paper, we describe a new way of examining frictional forces over the *entire* adhesive interaction between a scanning probe tip and the sample surface that not only avoids the inherent mechanical instabilities of spring-based sensors, but also completely decouples normal and lateral

force sensors. The experimental method is based on bringing together the techniques of shear-force microscopy [14, 15] and interfacial force microscopy (IFM) [16, 17]. With this arrangement, frictional forces acting to dampen the tip's lateral motion are monitored independently as a function of both positive (repulsive) and negative (attractive) loads. Thus the adhesive nature of friction at the earliest stages of contact can be clearly characterized. Initial results with a fluoro-silane adsorbed on silicon and two alkanethiols with chemically-distinct tail groups adsorbed on gold will be discussed. We will show evidence that strong chemical bonding at the free tail groups leads to frictional loss not only due to dissipative bonding forces at the contact interface, but also in part to tensile deformation and collective motion of the hydrocarbon chains.

A schematic of the experimental arrangement is shown in Fig. 1. It consists of a bare glass fiber mounted on a small "dither" piezo tube, which vibrates the fiber laterally, and a sample resting on an IFM sensor[16]. The sensor is mounted on a second, larger piezo (not shown) that is used for controlling the tip-sample distance and for scanning. The diameter of the glass probe tip is reduced to <100 nm by using a commercial puller [18]. An IFM sensor consists of a teeter-totter-like common plate of a differential capacitor suspended by torsion bars above two identical gold pads fixed in a glass substrate, creating capacitances C_1 and C_2 in Fig. 1. Details concerning operation of the sensor may be found elsewhere [16, 19], and are only briefly summarized here. The position of the common plate is determined by an rf bridge circuit and is initially balanced by static voltages applied to the capacitor pads. The sensor is then placed under proportional-integral-derivative feedback control by a circuit that supplies voltages to one pad to counteract any error signal due to normal forces applied to the fiber tip. The normal force can be directly calculated with reasonable accuracy and precision (±20%) from the feedback voltage, the capacitances, and the static voltages, or it can be directly calibrated (with greater accuracy and precision) using a laboratory micro-balance [16, 19]. Unlike AFM cantilevers, the sensor is mechanically-stable, non-compliant, and completely decoupled from the lateral motion of the tip. (Such a non-compliant device is often referred to as a "fixed grips" apparatus [20].)

As in most near-field scanning optical microscopy configurations [21] employing "shear-force" feedback [14, 15], the optical fiber typically has a mechanical resonance at 25-50 kHz (for 2-3 mm lengths), and a Q-factor of ~100. The amplitude of the lateral motion is determined by $A_{piezo}Q$, where A_{piezo} is the dither piezo drive amplitude (see Appendix). The dither piezo is in turn driven by a sinusoidal voltage applied to one of four quadrants [22]. Fiber motion induces voltages on the piezo, which is detected on the remaining quadrants by a phase-sensitive lock-in amplifier [23]. A large, constant background is present due the dither piezo driving motion, but this is easily subtracted. Unless otherwise stated, we use an initial "free" lateral displacement amplitude of ~12 nm, and we are able to detect tip amplitudes <1 nm upon contact with the sample. Attenuation of the fiber amplitude upon interaction of the probe tip with the surface is the basis for our friction measurements and for shear-force feedback, which allows the tip to be scanned over the surface without damage to tip or surface. The shear force damping (friction force) is proportional to the quantity $(1-V/V_0)$, where V is the attenuated signal at a given displacement and V_0 is the unattenuated signal due to the free lateral amplitude prior to contact (see Appendix). For the initial 12 nm free amplitude, we estimate that the frictional force at complete damping is 18 nN (see Appendix). By keeping the initial free amplitude constant, we in effect use the *same range of friction force* (0-18 nN) for all the experiments discussed here.

An example of shear force damping vs. displacement is shown in Fig. 2, where zero displacement is arbitrarily set to be the point where friction is first detected. Independent piezo calibration was performed against a known 50 Å feature; we estimate the displacement is accurate to within 15%. Also shown in Fig. 2 is the corresponding phase shift of the tip amplitude vs. displacement, where V_0 is arbitrarily set by the lock-in amplifier to have a zero phase shift. We see that the phase shift correlates very closely with the shear damping (see Appendix). The maximum phase shift observed at 90% attenuation of the initial 12 nm amplitude is < 25°, thus the quantity $x=V\cos(\theta)$ measured by the lock-in is to a good approximation equal to the amplitude V for the whole attenuation range. It is important to note that due to the large background created by the dither piezo, the apparent phase shift measured directly with the lock-in is very small [23]. The

actual phase shift vs. displacement shown in Fig. 2 was obtained by independent measurement of the lock-in signals $x=V\cos(\theta)$ and $y=V\sin(\theta)$.

Three different samples were prepared. The first consisted of a fluorinated silane, $CF_3(CF_2)_5(CH_2)_2Si(Cl)_3$ (hereafter denoted FTS), vapor-deposited under anhydrous conditions onto a silicon (100) substrate held at 50° C. The substrate was previously cleaned and hydroxylated in a 7:3 H_2SO_4/H_20_2 solution and dried under nitrogen. From ellipsometry measurements, it was verified that no more than one monolayer was deposited. The second and third samples were self-assembled molecular monolayers of two alkanethiols having the same chain length but differing tail groups: $CH_3(CH_2)_{11}SH$ (hereafter denoted CH_3-thiol), and $COOH(CH_2)_{11}SH$ (hereafter denoted COOH-thiol). The substrates were 100-nm-thick Au films, vacuum evaporated onto a 10-nm-thick film of Cr on clean silicon (100). The self-assembly took place in 1 mM thiol solutions in ethanol over 24 hours at room temperature. The chemistry of the bare glass tip was not modified, thus the native OH groups interact with the molecular monolayers.

All experiments were done immediately following sample preparation and under an atmosphere of filtered, dry nitrogen (relative humidity < 8%). Water is expected to be present in monolayer quantities under these conditions; however, no capillary condensation was observed. Control of the microscope and data acquisition are through home-built electronics and software [24]. The same bare glass tip was used throughout the experiments discussed below. Charging precludes scanning electron microscopy (SEM) analysis of bare tip shapes and sizes. However, SEM analysis has been performed on dozens of tips created under identical pulling conditions and coated with a known thickness of Al. We have found that the tips are blunt (flat), with a radius that varies from 30-50 nm; model tip shapes resembling the SEM images will be discussed in the next section.

We show in Fig. 3 the simultaneous response of the IFM normal force sensor together with the lateral shear damping (friction) when the tip approaches each of the three different samples. From top to bottom, the samples are FTS, CH_3-thiol, and COOH-thiol. The same tip and sensor is used throughout, and the same approach displacement rate of 2.5 Å/sec is used. The experiment is controlled by the degree of lateral damping; *i.e.*, when the attenuation becomes greater than a preset

value (80% of the undamped 12 nm amplitude), the tip is withdrawn at the same rate as the approach (for the sake of clarity, we do not show the withdrawal curves). As mentioned in the previous section, the same range of friction is explored in each case. We have also, like Fig. 1, arbitrarily set zero in the displacement axis to be the point where the damping (friction) begins.

In the top panel of Fig. 3, we see that as the lateral motion of the tip begins to be reduced by interaction with the FTS monolayer, the IFM sensor indicates an attractive (negative) load that reaches a maximum of -160 nN at ~15% damping and (-6±1) Å relative displacement. Thus it is clear that the initial shear force damping is due to *attractive* forces exerted on the probe tip. It is not until the lateral amplitude is reduced by ~60% of its initial free value that the load becomes positive, indicating a net repulsive interaction. As the load increases from the -160 nN value, the monolayer and substrate are compressed. The force-displacement relation in this ~18 Å compressive regime is consistent with the Johnson-Kendall-Roberts (JKR) model of elastic adhesive contacts [25] discussed further below. Indeed, a JKR force-displacement fit to the compression data provides an effective Young's Modulus of 12.9±3 GPa for this system, which is similar to 9.3±3.1 GPa previously measured for a supported thin hydrocarbon film [26]. Thus the mechanism(s) of lateral motion damping can have both attractive and repulsive components; however, it is clear that the first stage of friction is caused by attractive forces between the molecules and the tip before any compression of the film.

We can vary the initial attractive forces in a controlled way by examining the CH_3-thiol and COOH-thiol monolayers. In the middle panel of Fig. 3, we see from the initial IFM response to the tip interaction with the CH_3-thiol that there is a weak attractive interaction which reaches a negative load maximum of ~100 nN at a relative displacement of (-7±1) Å. As the tip continues the approach, the attractive interaction is overwhelmed by stronger repulsive forces that compress the CH_3-thiol monolayer and gold substrate. An effective Young's Modulus of 8.0±1 GPa is deduced for this system from the JKR force-displacement fit over the ~32 Å compressive region. Thus most of the shear damping in the CH_3-thiol case is due to repulsive forces on the tip, with only a small amount due to attractive forces.

In remarkable contrast to the CH_3-thiol, it is seen at the bottom of Fig. 3 that the tip interaction with the COOH-thiol is almost purely attractive; the tip motion is completely damped before appreciable repulsive compression can occur. In fact, the steep rise in friction with displacement and negative load suggests that a significant fraction of COOH-thiol chains undergo tensile deformation; *i.e., they "stand up" from their 30° tilt* [5] *to meet the probe.* This is schematically illustrated in Fig. 4, where on the left we show the strong tensile adhesive interaction of the COOH-thiols with the probe tip, and on the right we depict the compressive interaction with the CH_3-thiols. Like the CH_3-thiol, the maximum negative load (-300 nN) for the tip-COOH-thiol interaction is at a relative displacement of (-7±1) Å, although the attractive forces are clearly much stronger. By virtue of the stronger attractive interaction, COOH-thiols most likely adhere to the tip with enough force to collectively bring it to a halt. The collective motion of the chains will also act as an efficient channel for vibrational energy loss. Finally, the breaking of relatively strong adhesive bonds results in dissipative molecular motion and disordering, including chain entanglement and gauch defects [27]. Given the initial attractive regime, some of the ~18 Å long CH_3-thiol chains appear to stand up as well; however, they are unable to significantly slow the tip down because of the relatively weak attractive interaction. The ~12 Å long FTS chains also should undergo tensile deformation given the significant attractive interaction, although the initial tilt angle of the chains is unknown. For the densely-packed and ordered thiols, a tensile deformation of the layer in response to the attractive forces also requires over-coming the cohesive chain-chain van der Waals forces. This should be more difficult to do for the CH_3-thiol chains, relative to the COOH-thiol chains, because of the weaker attractive forces driving the deformation. Since cohesive forces increase with chain length, the likelihood of CH_3-terminated chains undergoing tensile deformation should decrease with increasing chain length. This idea may explain, in part, the AFM observation of decreasing friction force with chain length [7].

Thus we observe a considerable difference in the mechanisms of shear force damping strictly on the basis of adhesive interaction of the thiol tail group with the probe tip. The data from the FTS monolayer appears to exhibit both adhesive and compressive behavior. As discussed below,

the strong attractive interaction of the FTS monolayer relative to the CH_3-thiol is not expected given the low surface energy of fluorocarbon films [28, 29]. It should be mentioned that the corresponding withdrawal curves for Fig. 3 (not shown), usually exhibit some adhesive hysteresis with stronger adhesive forces than the approach curves. Poorly understood, adhesion hysteresis has been previously observed in both AFM [28] and SFA studies [4], and has been associated with interfacial energy loss between molecular films, including dissipative bond rupture.

In each of the IFM data sets in Fig. 3 we see that the tensile, attractive interaction between the tip and the tail groups extends from zero to ~(-7±1) relative displacement. Long range attractive interactions have been observed previously in normal force displacement curves [17, 30, 31], but we cannot, at this time, attribute the onset of *friction* to non-contact long range forces. Excitation of substrate phonons and electrons have been identified as dissipation channels [32, 33], however such forces are estimated to be considerably smaller than those lateral forces discussed here. We can account for ~3 Å range through the motion of the thiol chains from the initial 30° tilt to a 0° upright position. The additional ~4 Å could be due to surface roughness over the ±12 nm lateral motion. Another concern is that the tip may be slightly tilted with respect to the samples; this would result in a non-uniform surface interaction dominated by one turning point of its motion [34]. In this mechanism, the displacement range of shear force damping increases with free, initial amplitude, and the tip may have significant repulsive interactions with the substrate [34]. In our case, we see in Fig. 5A that as the free amplitude of the tip's lateral motion is reduced from 12 to 3 nm, there is no change in the displacement range of the shear force damping as it approaches the COOH-thiol surface. Thus we can conclude that the displacement range for the ±12 nm data is due solely to laterally-uniform adhesive interactions. The simultaneous IFM signals in Fig. 5B support this conclusion by indicating strong negative loads for each amplitude at comparable displacements. However, the strong potential well of the COOH-thiol/tip interaction is responsible for the steep and amplitude-independent displacement range of the shear forces. Given a high enough initial amplitude (>> 12 nm) to overcome the potential well, the displacement range would increase due to monolayer compression under positive loads. Indeed, when the shear force

amplitude dependence is repeated for the CH_3-thiol, higher loads (stronger repulsive forces) over longer displacement ranges are required to dampen the ±12 nm initial amplitude relative to the ±3 nm initial amplitude.

"Chemical force microscopy" has been identified as a means to utilize differences in adhesive forces as a contrast mechanism in AFM imaging [9, 10]. The results discussed above are consistent with the AFM contrast observed for the same thiols. However, it is important to note that due to the cantilever snap-to-contact instability, the AFM lateral force studies are restricted to *repulsive* contact or to the limited range of adhesive and repulsive interactions [12] prior to pull-off. We now demonstrate that the difference in purely attractive forces discussed above can also be resolved in images. We prepared a sample having a pattern of two thiols created by the technique of microcontact printing [35]. A polydimethylsiloxane stamp having 5.0 μm circles is "inked" with the CH_3-thiol solution (1 mM in ethanol) and applied to a clean Au-covered substrate for two minutes as discussed in Ref. [35]; un-stamped areas are then covered with the COOH-thiol by immersion in the 1 mM ethanol solution for 10 minutes. In Fig. 6A, we show a 6.0 μm image of the feedback signal required to maintain a constant shear force damping of 10%, which is in the region of attractive normal forces. When the tip is scanned from the CH_3-thiol region inside the circle to the COOH-thiol region outside, it must withdraw to maintain 10% shear damping under the stronger and steeper adhesive interaction. Thus the areas outside the circles in Fig. 6A are "higher" (brighter). The normal force signal from the IFM acquired simultaneously during the scan is shown in Fig. 6B. The IFM image is reversed relative to Fig. 6A because the COOH-thiol area produces a more negative (attractive) signal relative to the CH_3-thiol area (see Fig. 3). Thus, it is possible to map adhesive bond strengths in the *attractive regime* with this method. It is also clear from this experiment that shear-force feedback images commonly used to reveal "topologies" in near-field scanning optical microscopy [14, 15] can be misleading when different chemical constituents are present on the substrate.

Examination of the friction-load relation can yield considerable insight into the molecular mechanics of wearless friction, and can yield important parameters such as the work of adhesion

and the shear strength for a given interface. It was shown with the SFA [4, 36] that friction at low loads can be analyzed with the JKR [25] model of adhesive elastic contacts, which predicts the dependence of contact area upon the applied load, if one assumes that friction is proportional to the contact area through a constant shear strength (Eq. 1). The SFA technique has the advantage of measuring the contact area directly, whereas scanning probes do not. Despite this limitation, numerous AFM studies have successfully demonstrated that friction-load relations do reflect molecular properties such as chain length, molecular packing and tail group chemical identity [7, 37, 38]. Carpick *et al* [3, 39] have recently shown that the AFM single asperity contact can, in fact, be analyzed within the JKR formalism by once again assuming friction is proportional to contact area. For a parabolic tip-surface contact, the JKR relation of friction F, load L, and contact A is given by Eq. 1:

$$F = \tau A = \tau\pi\left\{\frac{R}{K}\left[L + 3\pi R\gamma + \sqrt{6\pi R\gamma L + (3\pi R\gamma)^2}\right]\right\}^{2/3}, \text{ where} \qquad (1)$$

$$K = \frac{4}{3}\left(\frac{1-\nu_1^2}{E_1} + \frac{1-\nu_2^2}{E_2}\right)^{-1}, \qquad (2)$$

and where R is the tip radius, τ is the shear strength which is assumed to be constant with load, and $\gamma$is the adhesion energy per unit area. The reduced modulus K of the two materials in contact (Eq. 2) is a function of the respective Young's moduli (E_1, E_2) and Poisson ratios (ν_1, ν_2) of the tip and sample. In our particular case, $E_2 \approx 70$ MPa and $\nu_2 = 0.4$ for glass [40]; from our load-displacement data, $E_1 \approx 13$ MPa for the silane covered silicon surface and $E_1 \approx 8$ MPa for the thiol monolayers on Au. If we assume that $\nu_1 \approx 0.4$ for the hydrocarbon films, then $K = 17$ MPa for the silane surface, and $K = 11$ MPa for the thiol surfaces. If R is known, a plot of friction vs. load can be used to determine both constants $\gamma$and τ. Extensions to Eq. 1 were developed by Ref. [39] to accommodate various tip shapes from parabolic to blunt. Specifically, for an axisymmetric tip approximated with height profile $z = cr^n$, we have from Ref. [39] the load relation

$$L = -(6\pi\gamma K)^{1/2}(A/\pi)^{3/4} + (3/2)Kcn\Psi(A/\pi)^{(n+1)/2}\ , \qquad (3)$$

where Ψ is a constant which depends on n. A corresponding equation relating displacement and contact area can be derived [41]. The height profile which gives the best approximation to our blunt glass fiber tip shapes and dimensions (based on SEM imaging) is $z=cr^4$, which is shown in Fig. 7 for c =10^{-6} and 10^{-5} nm^{-3}. Thus, with n=4, we have $\Psi = 8/15$ [39] and the following relations for load and displacement (δ) respectively:

$$L = -(6\pi\gamma K)^{1/2}(A/\pi)^{3/4} + (16/5)Kc(A/\pi)^{5/2}, \qquad (4)$$

$$\delta = -(8\pi\gamma/3K)^{1/2}(A/\pi)^{1/4} + (8/3)c(A/\pi)^{2}\ . \qquad (5)$$

The value for c is not adjustable for a well-characterized tip. However, uncertainty in our tip shapes forces us to fit the $F(=\tau A),L$ data to Eq. 4 for several values of c, and we find that c=10^{-5} nm^{-3} gives the best results. The determination of the reduced elastic modulus K mentioned previously involved numerically solving Eq. 4 and Eq. 5 simultaneously to eliminate A and fitting this relation to the load-displacement data in Fig. 3.

Fig. 8 shows the best fits of Eq. 4 to the same data that is plotted in Fig. 3. The fitting was done by parametrizing Eq. 4 in terms of the maximum negative load, or critical load L_c, and the corresponding critical friction F_c at this load, as discussed in detail in ref. [39]. From this, one can determine the critical contact area (A_c), the interfacial adhesion energy (γ) and the shear strength (τ)[39]. Since we estimate the maximum shear force at 100% lateral damping to be approximately 18 nN (see Appendix), we see for example at the top of Fig. 8 that for L_c = -160 nN, F_c $\approx$ 0.25×18 nN = 4.5 nN. A summary of the average adhesion energies (γ), shear strength values (τ), critical loads (L_c), *etc.*, over many data sets for each of the three different interfaces is given in

Table I. It should be noted that the small values of A_c (~400 nm^2), relative to the full tip geometry, are not unexpected given unresolved tip asperities and surface roughness.

For the CH_3-thiol we obtain γ and τ values which are in very close agreement with purely van-der-Waals-type molecular interactions [3, 4, 17, 29]. As expected, the COOH-thiol tip interaction has a much higher adhesion energy than that for the CH_3-thiol. If we subtract the 50 mJ/m^2 van der Waals contribution from 449 mJ/m^2, the result is close to the adhesive energy expected for hydrogen-bonding between the double-bonded O atom of the COOH group and hydroxyl groups on the glass tip. Assuming ~21 $Å^2$ per molecule surface coverage of the thiols [5] and a similar coverage of OH groups on the bare glass tip, we see that ~400 mJ/m^2 corresponds to a reasonable hydrogen bond strength of ~12 kcal/mole [17, 29]. (A water monolayer, if present on the COOH-thiol, is expected to give similar results). Thus we have a reasonable explanation for the attractive intermolecular forces acting on the tip for the two thiols. This is not the case for the FTS monolayer. Comparing the FTS and CH_3-thiol data in Table 1, we see that the work of adhesion is much greater for the FTS. It should be approximately the same, if only van der Waals forces are effective for the fluorocarbon-tip interaction. Indeed, recent AFM experiments have reported no difference in adhesion between CF_3- and CH_3-terminated thiols and a SiN tip, although a large increase in lateral forces was observed upon fluorination of the tail group [42]. The large value of γ for the FTS monolayer may be due to incomplete coverage with subsequent water contamination. Another possibility is a dipole-dipole interaction between the electronegative fluorines and the hydroxyl groups on the tip (i.e., a weak hydrogen bond). Clearly, more systematic studies, including tip functionalization, are required to understand this discrepancy.

Another unexpected and perhaps illuminating result is that the large differences in adhesive energies among the two thiols and the FTS is only mildly carried over to the respective shear strength values. We note, however, that the absence of data in the repulsive contact regime for the COOH-thiol due to the strong potential well of the attractive interaction could mean that the JKR fit provides only a lower bound to the estimated shear strength. At this time, there is no well-established relationship between shear strength and adhesion, yet it is clear from our data that

friction force is highly sensitive to adhesive energies. Much of what determines τ may be due to the structural and dynamical properties of the monolayers.

In the initial negative load regime prior to repulsive contact, which is available to us because of our mechanically-stable displacement-controlled approach, we see some deviation from the JKR fits. The JKR model assumes that the interfacial forces have zero spatial range, which is appropriate only for short-range forces. Thus it is clear that the negative load regime is not predicted for approaching surfaces by the JKR model. Long-range interactions are included in the alternative Derjaguin-Muller-Toporovan model [43]; however, this model predicts zero contact area at the critical load, which is incorrect for our data. Recent models [20] which allow a small, finite range to these forces predict that contact is first made with the surface displaced significantly upward under tensile stress from its equilibrium position; the resulting friction-load relations resemble those depicted in Fig. 8. Indeed, observing finite friction with such negative loads indicates that the materials have made contact under tensile stress and thus the "range" of attractive forces should take account of film deformation as the molecules extend upward in response to the attractive forces.

In summary, we have shown that the molecular origins of friction can be examined in detail with a novel instrument which features decoupled lateral and normal force sensors, and allows the complete adhesive interaction between tip and surface to be examined without jump-to-contact instabilities. Correlation of normal forces with lateral shear forces reveals both the adhesive and repulsive nature of friction between the contacting surfaces. We have been able to observe the simultaneous onset of friction and attractive forces, and show that chemical modification of the surface dramatically changes the attractive forces. An important insight gained from the initial experiments on self-assembled model lubricants is the significant energy loss, which steeply increases with attractive forces, that must be attributed to tensile molecular deformation, collective molecular chain motion, and dissipative bond ruptures. We have shown that selective area imaging under shear force feedback in the attractive regime allows one to map attractive forces with the IFM sensor. This is an advantage over AFM-based chemical force microscopy which detects lateral

forces while in repulsive contact. Finally, modeling of the friction-load relation within the JKR formalism allows us to see that the tip-surface interaction can be understood as a single asperity contact, and it allows us to quantify the work of adhesion and shear stress. However, limitations to the model due to finite-range attractive forces and modes of deformation unique to molecular films will require future study. Continuum mechanics can only be used as guide to the behavior we observe. Specific modes of molecular deformation could likely be identified by using approaches such as molecular dynamics modeling.

Table 1

Monolayer	L_c (nN)	γ (mJ/m^2)	A_c (10^{-16}m^2)	F_c (nN)	τ (MPa)
FTS	-161 ± 9	143 ± 13	3.5 ± 0.3	4.5 ± 0.2	12.9 ± 1.2
CH_3-thiol	-68 ± 20	50 ± 21	2.9 ± 0.8	4.0 ± 0.2	13.7 ± 1.5
COOH-thiol	-321 ± 25	449 ± 49	5.5 ± 0.1	10.9 ± 1.2	20.0 ± 1.9

Appendix

Following previous treatments [34, 44, 45], the vibrating NSOM tip can be modeled with a damped harmonic oscillator, which has the equation of motion given in Eq. A1:

$$m\ddot{y} + R\dot{y} + ky = F_0 e^{j\omega t} \quad . \tag{A1}$$

In Eq. A1, the effective mass of the vibrating fiber is m, the spring constant is k, the driving force is F_0 with frequency ω, and the damping coefficient is given by R. A solution to Eq. A1 is

$$y = Ae^{j(\omega t - \theta)} \quad , \tag{A2}$$

where A is the amplitude of the displacement y and θ is the phase lag between the drive force and the displacement. It can be shown that

$$A = \frac{F_0}{\sqrt{(k - m\omega^2)^2 + (\omega R)^2}}, \quad \text{and} \tag{A3}$$

$$\tan\theta = \frac{\omega R}{(k - m\omega^2)}. \tag{A4}$$

The maximum amplitude A_{max} at the oscillator resonance frequency ω_r is

$$A_{\max} = \frac{F_0}{R\sqrt{\left[\left(\frac{k}{m}\right) - \left(\frac{R^2}{4m^2}\right)\right]}} \quad \text{,where} \tag{A5}$$

$$\omega_r = \sqrt{\frac{k}{m} - \frac{R^2}{2m^2}} \quad . \tag{A6}$$

If $k/m >> R^2/4m^2$, then A_{max} can be approximated by

$$A_{\max} \cong \frac{F_0}{R\sqrt{\frac{k}{m}}} = \frac{F_0 Q}{k} = A_{piezo} Q \quad , \tag{A7}$$

where $A_{piezo} = F_0/k$ is the piezo drive amplitude, $Q=m\omega_0/R >>1$ is the quality factor, and $\omega_0 = (k/m)^{1/2}$ is the natural, undamped resonance frequency. Thus given the piezo-electric specifications and the measured Q, which is equal to the full width of the amplitude resonance at $A_{max}/\sqrt{2}$, the tip displacement at resonance can be estimated from Eq. A7. Absolute measurements of the tip displacement support this approximation [46].

Taking the real (steady-state) part of Eq. A2, we have for the fiber displacement y

$$y = A\cos(\omega t - \theta) \quad . \tag{A8}$$

The total damping (shear) force F_s, including both external and internal stresses, experienced by the fiber is given by

$$F_s = R\dot{y} = -RA\omega\sin(\omega t - \theta) = RA\omega\cos(\omega t - \theta + \pi/2) \quad . \tag{A9}$$

At resonance, the time-averaged damping force is then roughly

$$F_s \cong RA_{\max}\omega_0 = \frac{A_{\max}\omega_0^2 m}{Q} = \frac{A_{\max}k}{Q} \cong A_{piezo}k \quad , \tag{A10}$$

which is constant for a given driving force and is equal to the sum of the internal shear forces within the fiber (F_{int}) and the friction (F_f) due to the interaction of the tip with the sample. Thus as F_f increases, both A_{max} and Q decrease proportionally to maintain a constant F_s, which has been verified experimentally [44]. (From above, one also sees that A_{max} and Q are both proportional

to $1/R$). For a velocity-dependent damping force (where there are no force gradients), the resonance frequency will remain unchanged, provided $k/m >> R^2/4m^2$. (In tapping mode AFM there is a large force gradient, thus the cantilever experiences a frequency shift [47, 48].) Since A_{max} decreases with increasing F_f, the detected signal $V \propto A_{max}$ decreases, as does F_{int}. Thus we may estimate F_f from the following Eq. A11, where V_0 is the signal when the tip is not in contact with the surface:

$$F_f = F_s\left(1-\frac{F_{\text{int}}}{F_s}\right) \cong A_{piezo}k\left(1-\frac{V}{V_0}\right), \tag{A11}$$

Thus the quantity $(1-V/V_0)$ is directly proportional to the friction (shear force) at the tip, and values for F_f can be estimated from A_{piezo} and k. A_{piezo} is known for a given drive amplitude (although piezo constants may vary with drive amplitude), and the spring constant k can be calculated from the dimensions and material parameters of the glass fiber [40]. The spring constant will be affected somewhat by the taper of the tip [49], however, we assume for the present work a single value of k for the whole fiber. We estimate $k \cong 150$ N/m and $A_{piezo} = 0.12$ nm (for 100 mV drive); thus $F_f \cong 18$ nN at 100% signal attenuation.

To understand the close correlation between the phase shift and the amplitude damping shown in Fig. 2, we rewrite Eq. A4 as:

$$\tan\theta = \frac{\omega R}{m(\omega_0^2-\omega^2)} = \frac{\omega R}{m(\omega_0-\omega)(\omega_0+\omega)} \ . \tag{A12}$$

If $\omega \approx \omega_0$, and $Q = m\omega_0/R$, then

$$\tan\theta \approx \frac{\omega R}{m(\Delta\omega)(2\omega_0)} \approx \frac{\omega_0}{2Q(\Delta\omega)} \ . \tag{A13}$$

At resonance the phase shift between the drive force and the displacement is close to 90°, and $tan\theta \rightarrow \infty$. However, if the phase shift is measured by the lock-in amplifier in quadruture (θ-90°) then we have the situation where the measured phase shift is zero before tip encounters the surface, and it slowly increases from zero as the tip is damped. Since $tan\theta \cong \theta$, for $\theta < 20°$, we see that θ is inversely proportional to Q. We saw in Eq. A10 that Q and A_{max} decrease proportionally as F_f increases, therefore we expect to see a direct correspondence between $\theta < 20°$ and the amplitude.

References

1. J. Krim, Sci. Am. **275**, 74 (1996).
2. B. Bhushan, J. N. Israelachvili, and U. Landman, Nature **374**, 607 (1995).
3. R. W. Carpick and M. Salmeron, Chem. Rev. **97**, 1163-1194 (1997).
4. J. N. Israelachvili, in *Handbook of Micro/Nanotribology*, edited by B. Bhushan (Chemical Rubber Co., Boca Raton, 1995), p. 267.
5. L. H. Dubois and R. G. Nuzzo, Annu. Rev. Phys. Chem. **43**, 437 (1992).
6. J. Sagiv, J. Am. Chem. Soc. **102**, 92 (1980).
7. A. Lio, D. H. Charych, and M. Salmeron, J. Phys. Chem. B **101**, 3800 (1997).
8. N. D. Shinn, *et al.*, Langmuir **in press**.
9. C. D. Frisbie, L. F. Rozsnyai, A. Noy, M. S. Wrighton, and C. M. Lieber, Science **265**, 2071 (1994).
10. A. Noy, D. V. Vezenov, and C. M. Lieber, Annu. Rev. Mater. Sci. **27**, 381 (1997).
11. J. Peanasky, H. Schneider, and S. Granick, Langmuir **11**, 953 (1995).
12. R. G. Horn, J. N. Israelachvili, and F. Pribac, J. Colloid Interface Sci. **115**, 480 (1986).
13. D. F. Ogletree, R. W. Carpick, and M. Salmeron, Rev. Sci. Instrum. **67**, 3298-3306 (1996).
14. E. Betzig, P. L. Finn, and J. S. Weiner, App. Phys. Lett. **60**, 2484 (1992).
15. R. Toledo-Crow, P. C. Yang, Y. Chen, and M. Vaez-Iravani, App. Phys. Lett. **60**, 2957 (1992).
16. S. A. Joyce and J. E. Houston, Rev. Sci. Instrum. **62**, 710 (1991).

17. R. C. Thomas, J. E. Houston, R. M. Crooks, T. Kim, and T. A. Michalske, J. Am. Chem. Soc. **117**, 3830 (1995).

18. Sutter Instruments, Novato, CA

19. O. L. Warren, J. F. Graham, and P. R. Norton, Rev. Sci. Instrum. **68**, 4124 (1997).

20. J. A. Greenwood, Proc. R. Soc. Lond. A. **453**, 1277-97 (1997).

21. M. A. Paesler and P. J. Moyer, *Near Field Optics Theory, Instrumentation, and Applications* (John Wiley & Sons, Inc., New York, 1996).

22. The drive amplitude is 1.23 nm/volt for our EBL 1 tube, Stavely Sensors, East Hartford, CT.

23. J. Barentz, O. Hollricher, and O. Marti, Rev. Sci. Instrum. **67**, 1912 (1996).

24. The authors acknowledge the assistance of Brian Swartzentruber for both the electronics and the software.

25. K. L. Johnson, K. Kendall, and A. D. Roberts, Proc. Roy. Soc. Lond. A **324**, 301 (1971).

26. T. P. Weihs, Z. Nawaz, S. P. Jarvis, and J. B. Pethica, App. Phys. Lett. **59**, 3536 (1991).

27. A. R. C. Baljon and M. O. Robbins, Science **271**, 482 (1996).

28. N. A. Burnham, D. D. Dominguez, R. L. Mowery, and R. J. Colton, Phys. Rev. Lett. **64**, 1931 (1990).

29. J. N. Israelachvili, *Intermolecular and Surface Forces* (Academic Press, London, 1992).

30. G. S. Blackman, C. M. Mate, and M. R. Philpott, Phys. Rev. Lett. **65**, 2270 (1990).

31. N. A. Burnham, R. J. Colton, and H. M. Pollock, Nanotechnology **4**, 64 (1993).

32. E. Gerlach, Phys. Stat. Sol. B **176**, 365 (1993).

33. J. Krim, Com. Cond. Mat. Phys. **17**, 263 (1995).

34. M. J. Gregor, P. G. Blome, J. Schöfer, and R. G. Ulbrich, App. Phys. Lett. **68**, 307 (1996).

35. A. Kumar and G. M. Whitesides, App. Phys. Lett. **63**, 2002 (1993).

36. A. M. Homola, J. N. Israelachvili, M. L. Gee, and P. M. McGuiggan, J. Tribology **111**, 675 (1989).

37. J.-B. D. Green, M. T. McDermott, M. D. Porter, and L. M. Siperko, J. Phys. Chem. **99**, 10960 (1995).

38. M. T. McDermott, J.-B. D. Green, and M. D. Porter, Langmuir **13**, 2505 (1997).

39. R. W. Carpick, N. Agraït, D. F. Ogletree, and M. Salmeron, J. Vac. Sci. Technol. **B14**, 1289 (1996).

40. H. Muramatsu, N. Chiba, and M. Fujihira, App. Phys. Lett. **71**, 2061 (1997).

41. R. W. Carpick, in preparation .

42. H. I. Kim, T. Koini, T. R. Lee, and S. S. Perry, Langmuir **13**, 7192 (1997).

43. B. V. Derjaguin, V. M. Muller, and Y. P. Toporov, J. Colloid Interface Sci. **53**, 314 (1975).

44. K. Karrai and R. D. Grober, App. Phys. Lett. **66**, 1842 (1995).

45. Y. T. Yang, *et al.*, J. Appl. Phys. **81**, 1623 (1997).

46. C.-C. Wei, P.-K. Wei, and W. Fann, App. Phys. Lett. **67**, 3835 (1995).

47. R. Brandsch, G. Bar, and M.-H. Whangbo, Langmuir **13**, 6349 (1997).

48. N. A. Burnham, *et al.*, Nanotechnology **8**, 67 (1997).

49. P. K. Wei and W. S. Fann, J. Appl. Phys. **83**, 3461 (1998).

Figure Captions

Fig. 1 Schematic of experiment. A vibrating glass fiber with a tip diameter <100 nm is brought into contact with a sample resting on an IFM sensor. The sensor measures the attractive and repulsive normal forces on the tip by maintaining an electrostatic balance of two capacitances C_1 and C_2, formed by the common plate and identical gold pads fixed on a glass substrate (not shown).

Fig. 2 Shear damping and phase shift vs. displacement between vibrating (± 12 nm) bare glass tip and a monolayer of $CF_3(CF_2)_5(CH_2)_2Si(Cl)_3$ (FTS) on silicon. Zero displacement is arbitrarily set at the point of initial friction.

Fig. 3 Simultaneous shear damping of tip lateral motion (□) and normal forces (▲) on tip acquired for approach to FTS (top), CH_3-thiol (middle), and COOH-thiol (bottom) self-assembled monolayers. Zero displacement is arbitrarily set at the point of initial friction.

Fig. 4 Highly schematic representation (not to scale) of glass tip interaction with self-assembled thiols and silanes that are anchored to substrate. The upward arrow at left depicts the tensile molecular deformation under negative loads, that includes a re-orientation of the thiol chains from a ~30° tilt to a 0° tilt. The downward arrow at right depicts compressive deformation of the chains under positive loads. The extent of tensile stress, and ultimately that of friction in the lateral motion of the tip, is directly related to the strength of the attractive interaction that is depicted here as bonds between the tail groups and the OH groups on the tip.

Fig. 5 (A) Shear damping for various free, initial tip amplitudes: (●) 3 nm, (■) 6 nm, (▲) 12 nm. (B) Simultaneous IFM signals for shear force damping. The substrate is covered with COOH-thiol.

Fig. 6 Simultaneous 6.0 μm shear-force feedback (A) and IFM normal force (B) images of a patterned thiol monolayer. Inside the circle is CH_3-thiol , and outside the circle is COOH-thiol. In (A), bright (dark) areas indicate more (less) tip withdrawal by the scanning piezo to maintain constant shear-force damping. Whereas in (B), the bright (dark) areas indicate weaker (stronger) adhesive normal forces.

Fig. 7 Plots of $z=cr^4$, where $c=10^{-5}$ and 10^{-6} nm^{-3}, which most closely the resemble blunt glass tip shape used in the experiments.

Fig. 8 Johnson-Kendall-Roberts (JKR) fits to shear damping (friction) vs. normal load for the FTS (top), CH_3-thiol (middle), and COOH-thiol (bottom) monolayers. The data is the same as that plotted in Fig. 3.

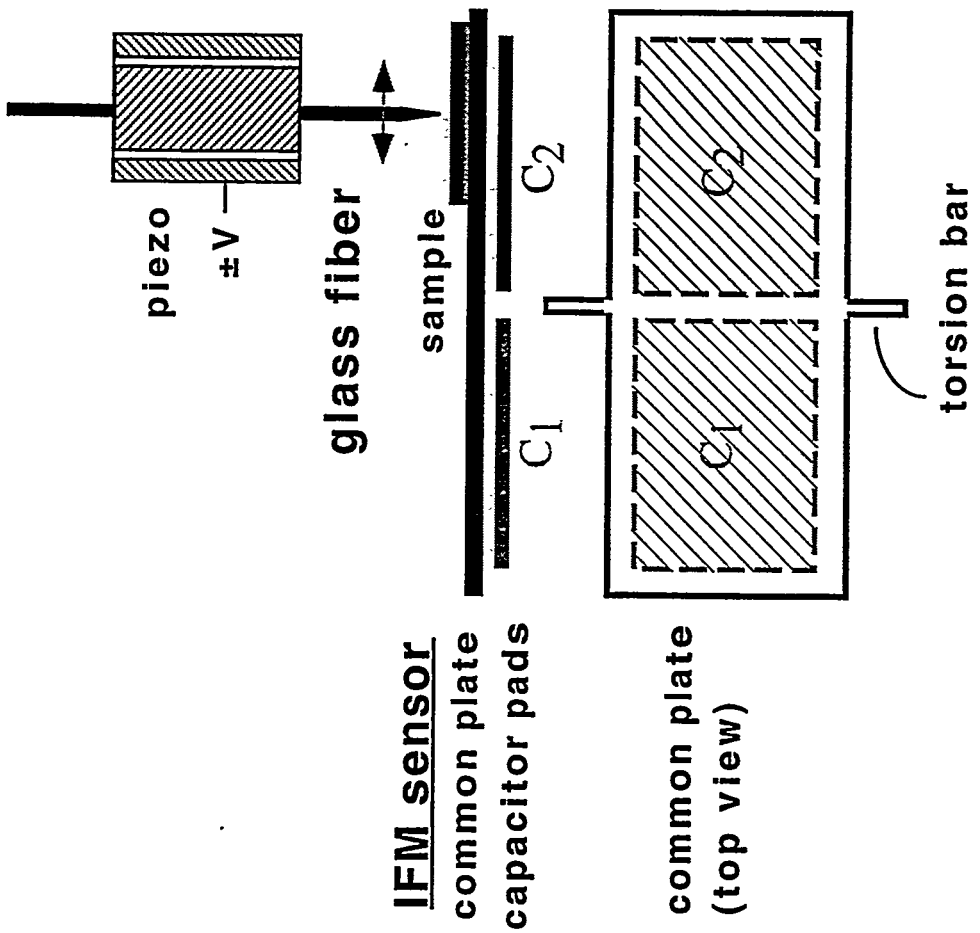
piezo
±V
glass fiber
sample
C_2
C_1
IFM sensor
common plate
capacitor pads
common plate
(top view)
C_2
C_1
torsion bar

Fig (1)

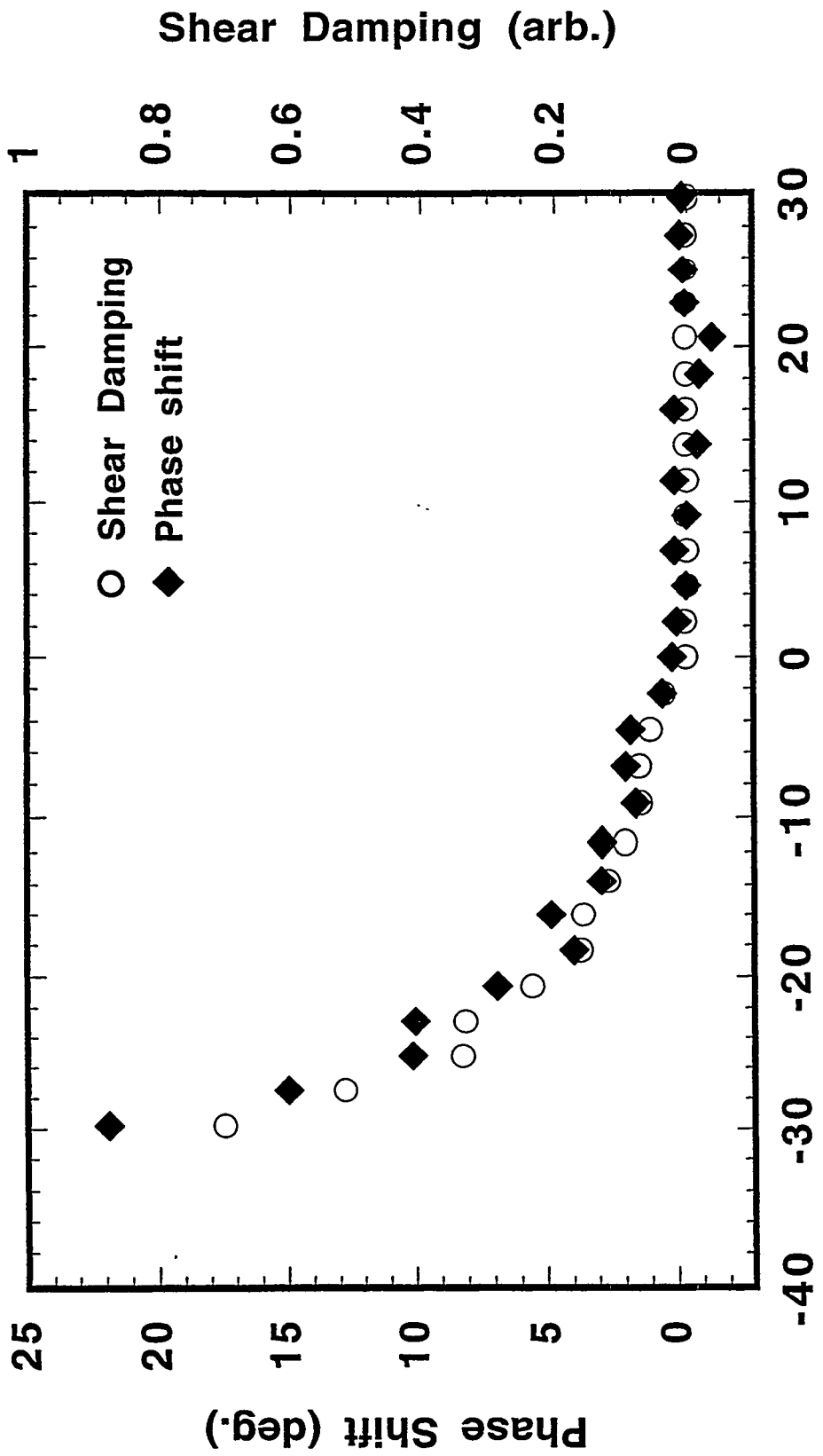
Shear Damping (arb.)
1
0.8
0.6
0.4
0.2
0
Shear Damping
Phase shift
30
20
10
0
-10
-20
-30
-40
Relative Displacement (Å)
25
20
15
10
5
0
Phase Shift (deg.)

Fig (2)

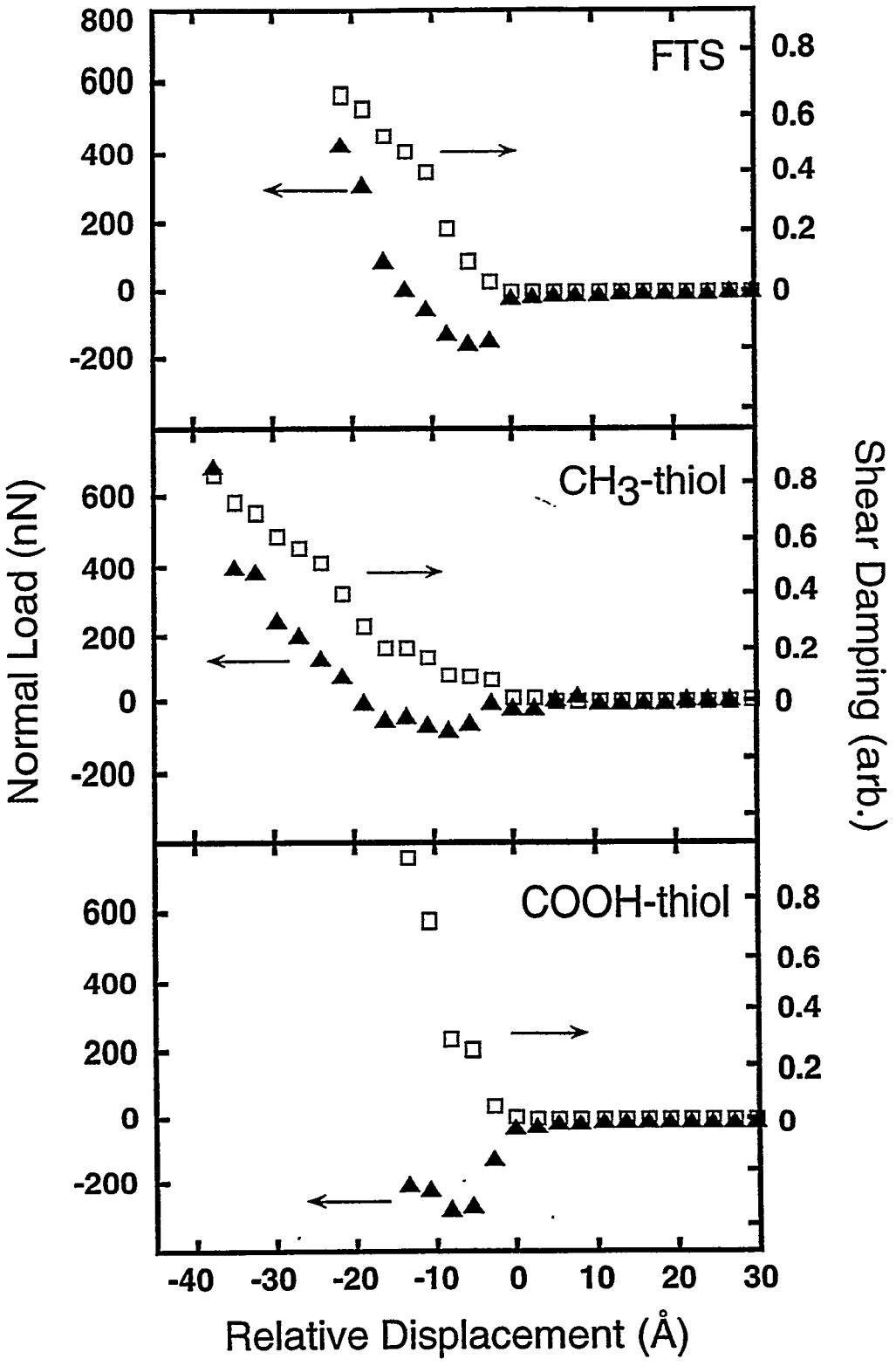
FTS
CH3-thiol
COOH-thiol
Normal Load (nN)
Shear Damping (arb.)
Relative Displacement (Å)
800
600
400
200
0
-200
0.8
0.6
0.4
0.2
0
-40
-30
-20
-10
0
10
20
30

Fig. (3)

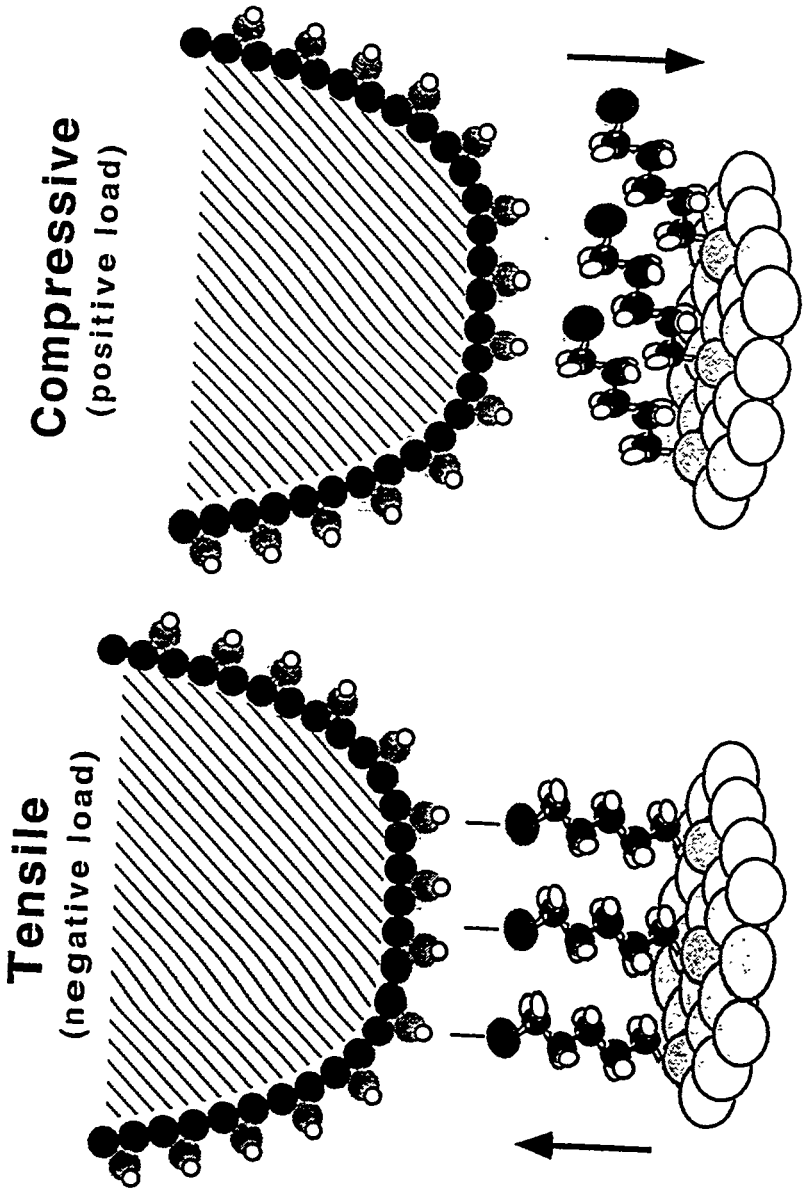

Fig. (4)

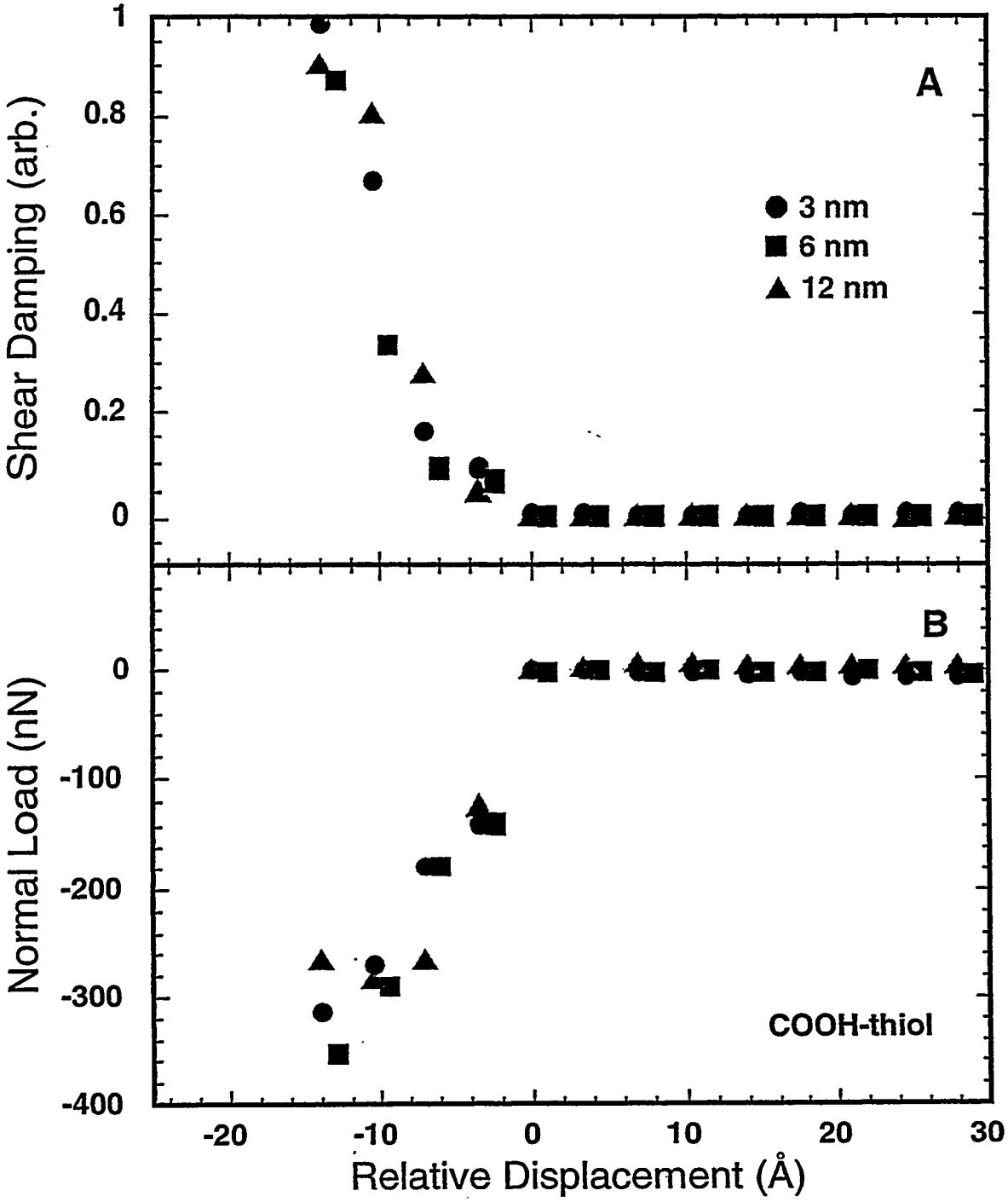
Shear Damping (arb.)
1
0.8
0.6
0.4
0.2
0
A
3 nm
6 nm
12 nm
Normal Load (nN)
0
-100
-200
-300
-400
B
COOH-thiol
-20
-10
0
10
20
30
Relative Displacement (Å)

Fig. (5)

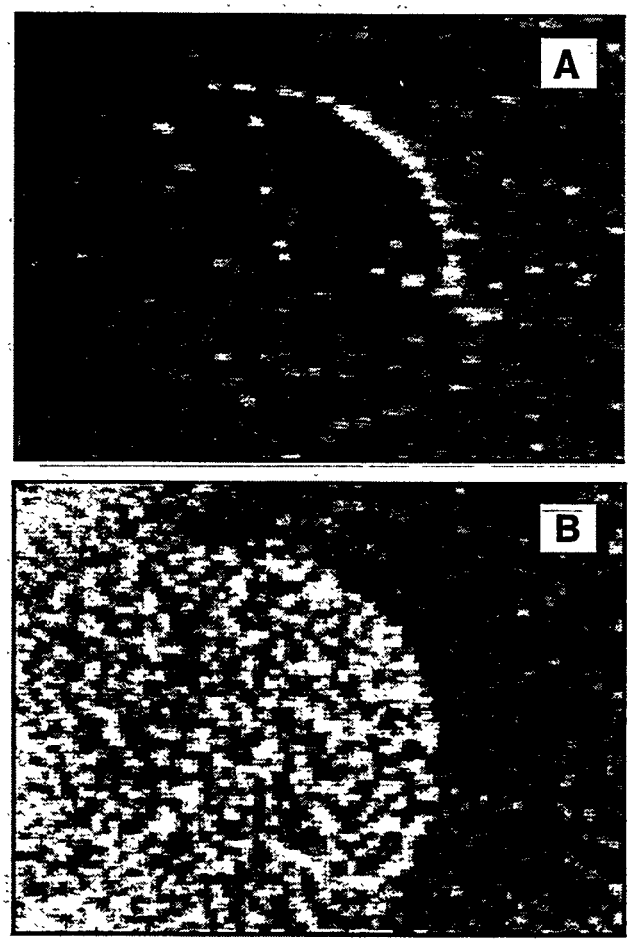

Fig. (6)

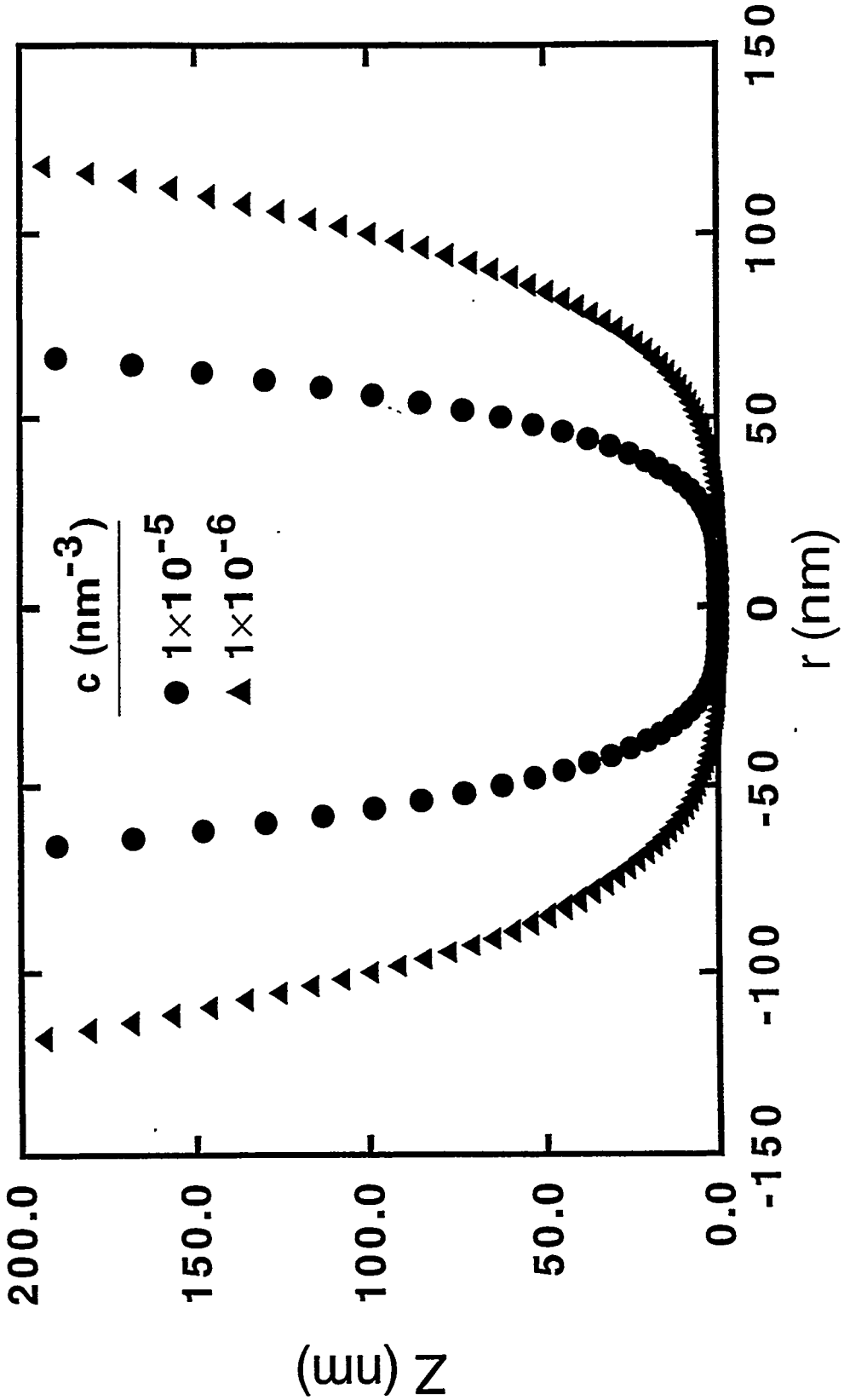
200.0
150.0
100.0
50.0
0.0
Z (nm)
-150
-100
-50
0
50
100
150
r (nm)
c (nm^{-3})
1×10^{-5}
1×10^{-6}

Fig. (7)

52e

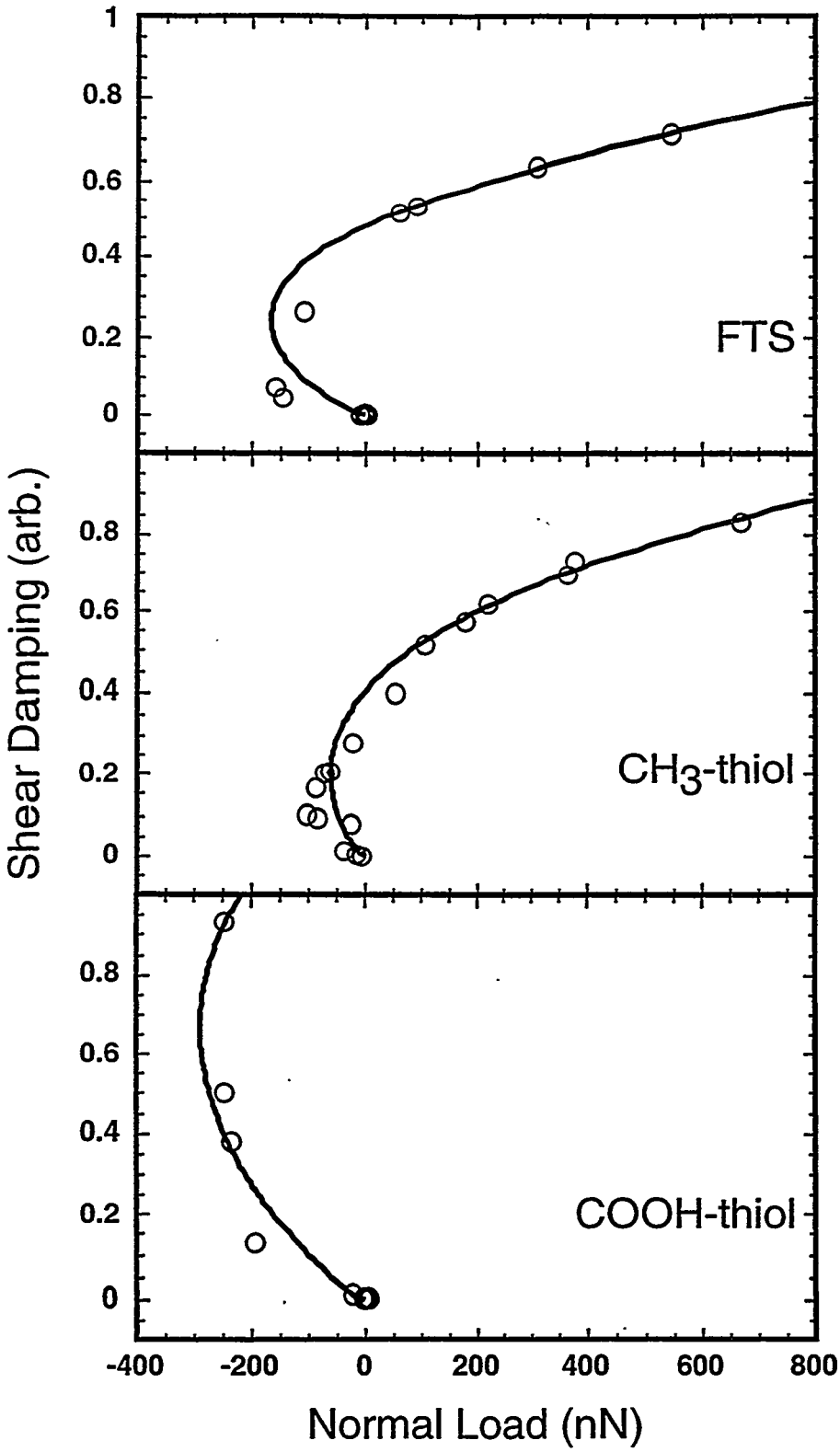
Shear Damping (arb.)
1
0.8
0.6
0.4
0.2
0
FTS
CH3-thiol
COOH-thiol
-400
-200
0
200
400
600
800
Normal Load (nN)

Fig (8)

3. Silane Deposition, Characterization, and Tribology (Dugger)

Surface micromachined electromechanical devices on silicon substrates represent a popular fabrication route to MEMS, due to the infrastructure and process knowledge available from the semiconductor industry. Although the number of materials compatible with silicon surface micromachining is large, material selection may be constrained by process temperatures or chemical compatibility, particularly in cases where the micromachine is to be integrated with CMOS logic. Surface treatments can be used to improve interfacial properties where the composition of the structural elements is constrained.

Adhesion between polycrystalline silicon members or the substrate (referred to as "stiction") can lead to failure of microelectromechanical systems. This adhesion can occur during processing, when the hydrophyllic surfaces present after wet chemical release etching are dried in air and capillary forces bring the surfaces into contact (Pietsch et al., 1994). Adhesion may also occur in use, between surfaces left in contact for long periods of time or brought together by mechanical shock. Mastrangelo (1997) discussed the mechanisms of adhesion-related failure, and suggested that low energy monolayer coatings, such as silane films, are the most effective and reliable adhesion prevention methods. Maboudian and Howe (1997a, 1997b) reviewed several methods for adhesion reduction including chemisorbed molecular monolayer coatings, concluding that back-end processes such as packaging are likely to limit the applicability of adhesion reducing treatments, and more work is necessary to understand the impact of these surface treatments on friction and wear.

Micromachined electomechanical devices of interest to Sandia National Laboratories can have complex mechanical interfaces, with many kinds of relative motion between structures including impact, rolling, and sliding. We are investigating surface treatments to improve the friction and wear behavior of MEMS. The relationship between surface preparation, processing, and performance of chemisorbed alkylsilanes on silicon is the subject of this paper.

Flat coupons for silane deposition were 1×1 or 2.5×2.5 cm squares cleaved from virgin p-type (100) wafers. The coupons were either bare silicon or silicon coated with a ~ 2 _m thick

polycrystalline silicon film deposited by low pressure CVD. Coupons were loaded into crystal carriers (Fluoroware® perfluoroalkoxy) for wet chemical treatment.

A variety of wet chemical surface preparation and post-cleaning drying techniques were used in an attempt to vary the surface chemistry and amount of physisorbed water available to participate in reactions with the silane head group. These generally consisted of cleaning (H_2SO_4:H_2O_2 mixtures from 10:1 to 2:1 at ~110°C due to exothermic reaction heat only), oxide etching (H_2O:HF:HCl mixture of 10:1:0.1 at room temperature), and oxide regrowth (H_2O:NH_4OH:H_2O_2 mixture of 20:1:1 at 45°C) solutions. All chemicals were analytical reagent and low particle count electronic grades. Filtered high purity deionized water was used in solutions as well as for rinsing between the treatment steps. Times in these solutions were generally 10, 5, and 10 minutes, respectively.

In addition to wet chemical methods, some coupons were exposed to UV-ozone to insure complete oxidation and hydration of the silicon surface. Coupons were held within 1 cm of a UV lamp for 1 hour.

Coupons were either dried in laboratory air on a clean bench, oven dried at 120°C for 1 hour, or transferred to the coating solution by solvent exchange. Coupons dried in the oven were moved between the oven and coating stations in a glass desiccator with minimal exposure to the ambient atmosphere. Coupons transferred to the coating solution by solvent exchange were moved from solution to solution, in the following sequence after the release and cleaning steps above: H_2O→isopropyl alcohol→1,1,2-trimethylpentane (anhydrous)→coating solution.

Octadecytrichlorosilane ($C_{18}H_{37}SiCl_3$) and perfluorodecyltrichlorosilane ($C_{10}H_4F_{17}SiCl_3$) (95%, Acros) were vacuum distilled prior to preparation of coating solutions. Vacuum distillation was carried out at a pressure lower than 2.7 Pa, and high purity argon was used to purge the distillation apparatus prior to capping the receiver flask. The distilled silane was immediately moved to a glovebox purged with dry nitrogen, for storage and preparation of coating solutions.

Coating solutions consisted of 1 mM silane in organic solvent. Anhydrous toluene, hexadecane, or mixtures of hexadecane with CCl_4 or chloroform were used to prepare coating solutions within a nitrogen purged glovebox. Solution volume was typically 400 to 700 ml in a

perfluoroalkoxy tank, and samples were transferred to the tank in the same crystal carriers as used for substrate preparation. To examine the effect of treatment time on silane coverage, coupons were moved after various times in the coating tank to a carrier in a rinse tank which contained only the solvent. After all coupons had been moved, the rinse tank was removed from the glovebox and the carrier transferred to an alcohol bath. Coupons were ultrasonically cleaned in two successive alcohol baths for 10 minutes each, and then allowed to dry on a clean bench.

Several techniques were used to examine the silane coatings prior to tribological tests. These surface treatments create a hydrophobic surface and are effective in reducing adhesion between elements due to capillary attraction (Srinivasan, et al., 1997). Static water contact angle measurements were performed on all treated surfaces as a qualitative indicator of coating coverage. A 3 to 6 _l drop of water was placed on the surface, and a side view of the droplet on the surface was captured immediately using a CCD camera and video frame grabber. Digital image analysis was used to determine the shape of the static droplet and the contact angle with the surface.

Time-of-flight SIMS (TOF-SIMS) was used to determine the amount of silane present on the surface, as well as the concentration of contaminants in the film or on the substrate. A PHI_TRIFT spectrometer was used, which employs a 15 keV pulsed Ga ion beam rastered over an area of ~90×90 _m. Collection time was on the order of 1 minute. Dosage during data collection was on the order of 10^{11} ions. For comparison of the silane coverage with different treatment processes, the ratio of the C_3H_7 peak to the $SiCH_3$ peak was used. C_3H_7 is an ionization fragment of the silane molecule, and $SiCH_3$ is from the head group. Both of these peaks are of comparable intensity and occur near mass 43, thus minimizing instrument sensitivity corrections.

Macroscopic friction between treated Si(100) flats and polished semiconductor grade SiO_2 balls (Hoover) was measured using an ICS-200 pin-on-disk tribometer (Falex Corporation). A normal load of 10 gf and sliding speed of 2 cm/s was used for all experiments. The friction force was captured at a rate of 5 Hz, and sliding continued until a friction coefficient above 0.5 was observed, accompanied by visible damage to the Si flat.

Samples of Si(100) or blanket polycrystalline silicon on Si(100) were examined in a scanning probe microscope (Park Scientific Instruments Autoprobe LS) using an etched silicon probe. Probes were untreated, and had a nominal radius of curvature of 10 nm. Imaging forces measured by the deflection of the cantilever (Ultralever 'B' with normal spring constant of 0.24 N·m) were between 30 nN compressive and 5 nN tensile.

Figure 1(a) shows water contact angle as a function of coating time for ODTS films formed using a variety of surface preparation techniques and deposition solutions. The data show that after about 100 minutes, all deposition processes result in a hydrophobic surface. The rate at which contact angle increases with treatment time varies with process at short treatment times. In Figure 1(b), the coverage of silanes has been measured as a function of coating time for the same samples as in Figure 1(a), but using SIMS peak area ratios as a measurement of coverage. Large differences in the amount of silane on the silicon surface as a function of process and treatment time can be seen in Figure 1(b).

In Figure 2, the data in Figure 1 is plotted as contact angle as a function of silane coverage as measured by SIMS. This figure shows that at coverages above that required to produce a hydrophobic surface, the water contact angle is not a sensitive measurement of the amount of silane on the surface. Water contact angle is frequently used as a qualitative measure of coating integrity when depositing silane films for adhesion reduction in micromachines. The important result of this data is that silane-treated surfaces which are hydrophobic may have dramatically different amounts of molecules adsorbed on the surface, which may be expected to exhibit different friction and wear behavior. Therefore, while contact angle may be sufficient to determine when micromachine surfaces are hydrophobic to prevent adhesion of structural elements, a more quantitative measure of coverage is required to insure surfaces with consistent tribological behavior.

Macroscopic friction tests were performed on coated Si(100) samples in contact with polished balls of semiconductor grade SiO_2. Sliding tests were performed in laboratory air at 11% relative humidity. Figure 3 shows the relationship between friction, coating durability, and ODTS coverage measured by SIMS. The initial friction coefficient was determined for the first few cycles

of sliding, before damage to the substrate had occurred. The figure shows that the starting friction coefficient decreases monotonically as the amount of ODTS on the surface increases. As a qualitative measure of the ability of the coating to protect the silicon surface, the number of sliding cycles required for the friction coefficient to exceed 0.2 was determined and is also plotted in Figure 3. This data also shows a monotonic dependence on ODTS coverage. In short, the macroscopic friction tests on ODTS-coated Si(100) as a function of coverage show that both the initial friction and the ability of the coating to protect the surface depend on the amount of silane chemisorbed on the surface. Therefore, while all of these surfaces are hydrophobic, they might be expected to exhibit different tribological behavior at microscale contacts depending upon the actual coverage of the ODTS.

Scanning probe microscope experiments have been conducted to determine how chemisorbed ODTS films respond to compressive and shear stress in a single asperity contact. Films of a variety of coverages have been examined using conventional AFM cantilevers with silicon probes, and both topography and lateral force images are typically acquired simultaneously. Figure 4 shows the results of a typical experiment of this type. We begin by scanning the probe over the treated Si(100) surface at constant applied force to create an area ~ 2 _m square that has been contacted by the probe. Additional areas may be created nearby using different contact parameters. After several areas have been scanned by the probe, we then increase the size of the scan and make a single pass over the previously scanned areas while simultaneously measuring the vertical and torsional displacement of the cantilever. The results are shown in Figure 4(a), which is a lateral force image from the first pass of the probe, that includes areas that were previously scanned 3 times by the probe. For some ODTS films, we find a change in the lateral response of the film after scanning. The signal from the lateral force detectors has been mapped to color in the image so that red represents high force, and blue represents low force. Therefore, the areas previously scanned exhibit lower lateral force than those scanned for the first time. The topography image acquired simultaneously shows no significant change in height that accompanies this change in lateral force response. Figure 4(b) shows that while the topography is unchanged compared to the

surrounding area, the lateral force for previously scanned areas is decreased, whether the area is scanned under compressive or tensile force. Much more research is required to understand the mechanism for this change in lateral force with rubbing, and how it depends upon the molecular configuration of the coating. However, we hypothesize that scanning of the coated surface facilitates alignment of the ODTS molecules, which would tend to increase van der Waals interactions between the chains. Increased van der Waals interactions would stiffen the film, and reduce the vibrational and rotational modes available to the molecules to dissipate energy. The friction coefficient of the aligned regions would therefore be expected to be less than that in regions that have not yet been aligned by shear.

Formation of dense films of ODTS on silicon is not a trivial process. Large variations in the kinetics of film formation are exhibited depending upon how the surfaces are prepared for coating deposition. While all the surface preparation processes investigated in this work allowed hydrophobic surfaces to be produced within about 60 minutes of exposure to the coating solution, quantitative measurement of the ODTS coverage by SIMS indicates that large variations in coverage are still present. While these variations in coverage may not significantly impact the performance of devices that are designed to prevent the contact of silicon surfaces, other devices which rely on the contact of surfaces are expected to exhibit performance that is dependent on the details of the surface treatment process.

Macroscopic friction measurements between untreated SiO2 balls and ODTS treated Si(100) flats show that the friction and durability of these surfaces are directly related to the quantity of ODTS chemisorbed on the surface. Friction decreases and the number on sliding cycles required for the friction coefficient to exceed 0.2 increases as the coverage of ODTS increases.

A change in the lateral response of ODTS films to shear after repeated contact has been observed in scanning probe microscope experiments. A hypothesis consistent with the observed decrease in friction response after rubbing has been developed. Orientation of the adsorbed molecules by rubbing, resulting in increase van der Waals attraction between molecules and reduced deformation modes on subsequent contact, is believed to be responsible for the observed

changes. Further scanning probe work, making use of the new tools which have been developed, is required to verify this hypothesis.

References

Maboudian, R. and Howe, R.T. (1997a) Critical Review: Adhesion in Surface Micromechanical Structures, *J. Vac. Sci. Technol.* **B15**, 1-20.

Maboudian, R. and Howe, R.T. (1997b) Stiction Reduction Processes for Surface Micromachines, *Tribology Letters* **3**, 215-221.

Mastrangelo, C.H. (1997) Adhesion-Related Failure Mechanisms in Microelectromechanical Devices, *Tribology Letters* **3**, 223-238.

Pietsch, G.J., Kohler, U. and Henzler, M. (1994) Chemistry of Silicon Surfaces After Wet Chemical Preparation: A Thermodesorption Spectroscopy Study, *J. Vac. Sci. Technol.* **B12**, 78-87.

Srinivasan, U., Houston, M.R., Howe, R.T., and Maboudian, R. (1997) Self-Assembled Fluorocarbon Films for Enhanced Stiction Reduction, *Transducers '97*, Chicago, Illinois, June 1997, pp.

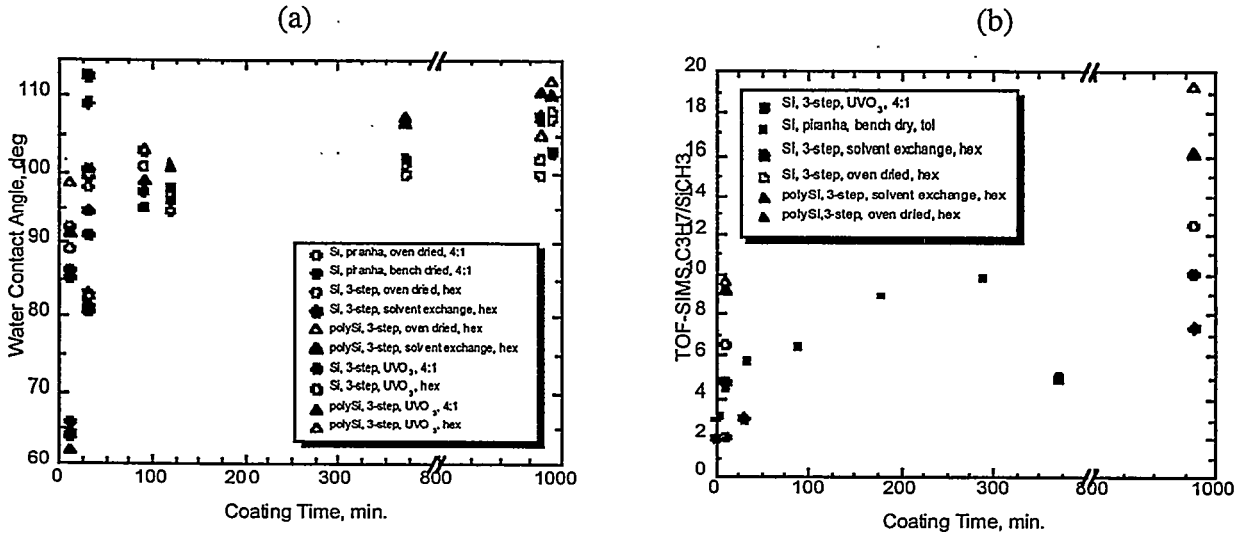

Figure 1. Water contact angle as a function of coating time (a) for deposition of ODTS from 1mM solutions with a variety of surface preparation techniques. The coverage of ODTS measured by SIMS is plotted for select samples in (b).

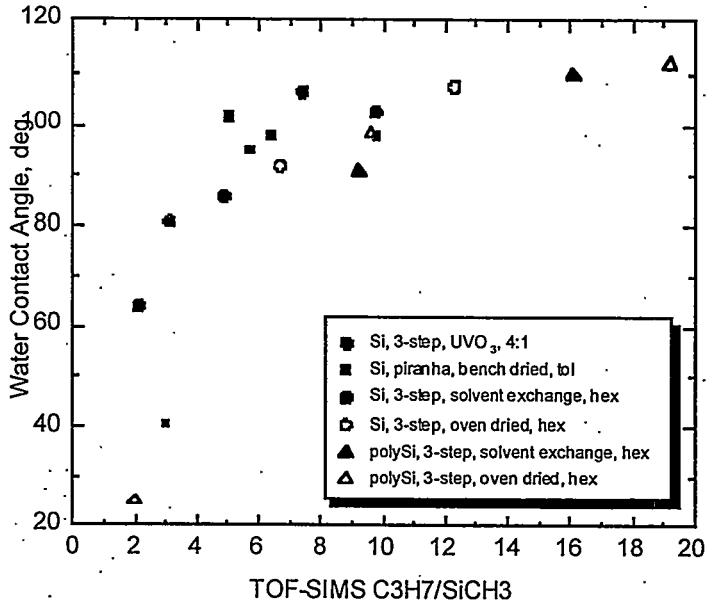

Figure 2. Water contact angle as a function of ODTS coverage measured by SIMS.

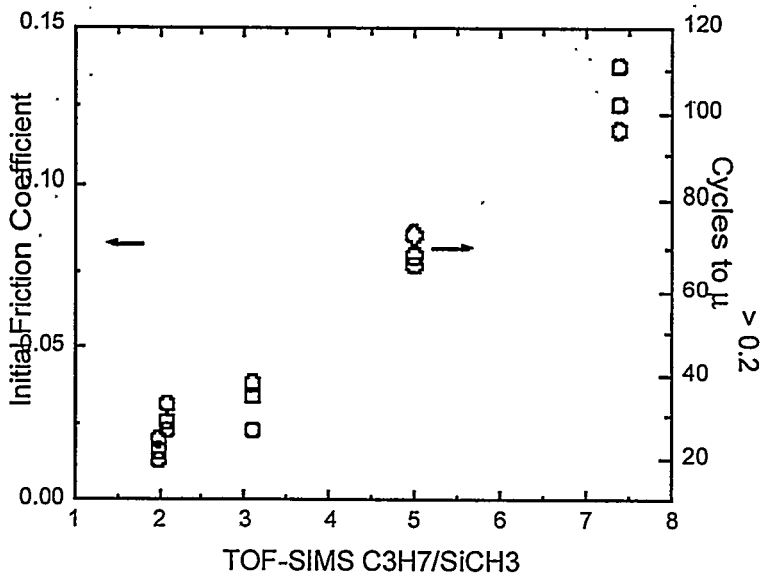

Figure 3. Friction and durability of ODTS films as a function of coverage for macroscopic ball on flat tests.

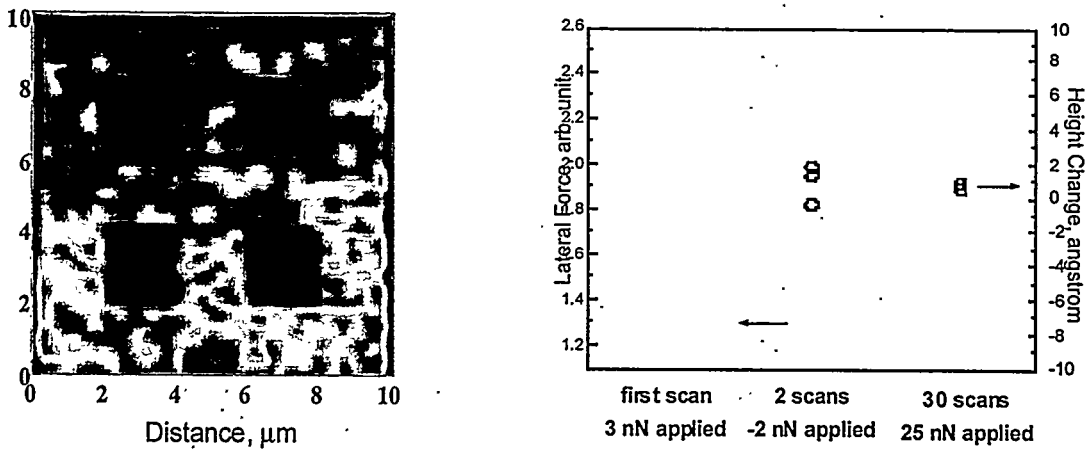

Figure 4. Lateral force image (a) showing comparison of previously scanned areas ~ 2 _m in size and the surrounding area scanned for the first time. The top squares were scanned at a compressive load of 25 nN, while the bottom squares were scanned with a tensile load of 2 nN. In (b) the lateral force and topography for areas previously scanned are compared to the surrounding region scanned for the first time.

4. Compositional Characterization of Microcontact-Printed SAMs Formed From Octadecyltrichlorosilane (Zhou, Lopez, Burns)

Self-assembled monolayers (SAMs) formed from octadecyltrichlorosilane ($Cl_3Si(CH_2)_{17}CH_3$, OTS), on silicon-silicon dioxide substrates have been prepared by adsorption from dilute solutions under dry nitrogen conditions for different exposure time. These SAMs were characterized by ellipsometry, wettability, Lateral force microscopy (LFM), X-ray photoelectron spectroscopy (XPS) and Fourier transformation infrared spectroscopy (FTIR). A consistent growth behavior was observed for octadecylsiloxane monolayers on Si wafer by all the applied techniques. Analysis of relative friction measured for the SAMs formed with different exposure time suggests that LFM can be used as a semiquantitative technique for compositional mapping of the surface coverage of SAMs. Correlation between relative friction and the surface coverage of octadecylsiloxane estimated by XPS and FTIR is presented for the SAMs investigated. This correlation and LFM imaging were used to estimate the surface coverage of octadecylsiloxane in microscopic pattern areas formed by microconatct printing on silicon wafer.

Self-assembled monolayers (SAMs) of alkylsiloxanes has been considerable interested in recent years. These organosilane films terminated with various functionalized groups are used in various fields, such as molecular electronics,[1] lubricants,[2] biosensors,[3] protein and polymer adhesion.[4,5,6] Microcontact printing (μCP) has been used to create patterned surfaces of organosilanes[7] that allow the facile tailors of the physical, chemical and biological properties of surfaces and the study of many interfacial phenomena, including etching,[8] biorecognition,[9] heterogeneous nucleation,[10] protein[4] and cellular adhesion,[11] and deposition of conducting polymers.[12] With increased of application of self-assembled monolayers, the ability to determine the molecular arrangement and composition of SAMs is a matter of increasing importance. A number of techniques have been applied to characterize SAMs formed both from solutions and by microcontact patterning, such as XPS,[13] scanning electron microscopy (SEM),[14] secondary ion mass spectroscopy (SIMS),[15] analysis of condensation figures,[16] and Fourier transformation infrared spectroscopy - attenuated totally reflectance (FTIR-ATR).[17] Traditional atomic force

microscopy (AFM) has been successfully exploited for imaging SAMs growth on atomically flat substrates.[18-20] Lateral force microscopy (LFM) provides images of patterned SAMs,[21-24] chemically-distinct domains[25] and composite organic films.[26] LFM has also been being used for measuring friction, shear and adhesion properties of monolayers,[27-30] which are important in many applications including lubrication,[2,30] tribology[31,32] and recognition in biological systems.[9,13,33] A LFM method applying LFM to semiquantitatively characterize alkenthiol monolayers by correlation of surface friction and image contrast to the composition was developed in our laboratory.[34] The purpose of this work is to further develop the LFM technique for semiquatitative characterization of surface coverage of octadecylsiloxane ($O_3Si(CH_2)_{17}CH_3$, referred to herein as SiC18) in SAMs formed from solution of OTS in hexadecane. The LFM technique is relatively cheap and simple when compared to XPS, SEM and SIMS, while both normal FTIR and FTIR-ATR are limited to IR transparent substrates. In addition, XPS, FTIR, SEM and SIMS measure the average information over a larger measurement area then LFM does. LFM, as a local probe technique, should be more appropriate to determine local structure and growth of SAMs. It is convenient for the investigation of chemical features of patterned organic surfaces, also has the potential application in imaging surfaces with high lateral resolution, with good resolution in detecting the chemical composition and coverage of patterned surfaces.

Octadecyltrichlorosilane was purchased from Sigma Inc. and was vacuum distilled and collected under nitrogen prior to use. 1mM solutions of OTS in Aldrich hexadecane was prepared in a glove box filled with dry nitrogen. The substrates (about 1cm x 1cm) for the SAMs were cleaved from a silicon wafer cleaned with Piranha etch, a mixture of 30% hydrogen peroxide and 70% sulfuric acid, followed by deionized water rinse and nitrogen blow dry. (CAUTION: Piranha solution reacts violently with organics. Be extremely careful in handling it.) All exposures to form the SAMs were conducted in a glove box under a dry nitrogen environment for the specified exposure time, and then the substrates were transferred to pure heptane followed by an ultrasonic cleaning in methanol to remove excess silane aggregates from the surface. The patterned samples

were formed by microcontact printing by PDMS stamps inked with the same solution and then cleaned by the same procedures as used for samples formed from solution.

Thickness measurements were conducted using a multiwavelength ellipsometer (Model M-44, J. A. Woollan Co., Inc.). Si and native SiO_2 models were chosen for pure Si wafer and a Cauchy model was chosen for SAMs on the Si wafer to fit the experimental data of psi and delta, and yield the film thickness. Three measurements in different parts on surface were conducted for each sample. A Rame-Hart Model 100-00 contact angle goniometer equipped with a video monitor was used to measure advancing contact angles of deionized water for the SAMs formed on the substrates with different exposure time. Three contact angles were recorded in three points on each sample surface.

A Nanoscope III from Digital Instrument Co. was used for LFM imaging and relative friction measurements of patterned and unpatterned SAMs surfaces. A 200 μm narrow-legged standard triangle silicon nitride cantilever was chosen to get large lateral deflection signals. Scope mode of LFM was used for acquiring friction data as described in our previous article.[34]

X-ray photoelectron spectra of unpatterned and patterned SAMs were acquired using a Kratos Analytical AXIS-Hsi system with monochromatized Al Kα radiation and the detector at an angle of 45°. Binding energy for calibration of the instrument is referenced to the Ag 3d5/2 peak at 368.3eV.[35] The ratio of the area under C 1s peak at 284.7 eV to the area under SiO_2 component in Si 2p peaks at 103 eV and 101.7 eV , corrected with relative sensitivity factors[35] was used to calculated relative concentration of SiC18 for each sample. An estimate of surface coverage of SiC18 was obtained by the relative concentration.. FTIR spectra were obtained using a Perkin-Elmer Spectra 2000 Fourier transform infrared spectrometer with a MCT detector cooled with liquid nitrogen. The system was purged with dry nitrogen for 2 hours prior to measurement. The total integrated intensity under the peaks corresponding to the $\nu_s(CH_2)$ symmetric stretching mode at ~2850 cm^{-1} and the $\nu_{as}(CH_2)$ asymmetric stretching mode at ~2918 cm^{-1} was used to estimate the surface overage of the SiC18 on the silicon substrates for various samples formed with different exposure time.

Figure 1 shows that the thickness (top) and contact angles (bottom) of the SAMs of SiC18 on Silicon wafer from solution with the different exposure time. In a preliminary experiment, the same set of samples for each exposure time were used for both thickness and contact angle measurements as comparison to observe growth behavior of the SAMs. A consistent behavior of the SAMs formation was observed by the two techniques. Later on, for each exposure with different time, two sets of samples were prepared concurrently through the entire exposure process. One set of samples were used for ellipsometric, FTIR and LFM measurements, the other set were used for contact angle and XPS measurements. The two sets of samples are comparable each other, due to consistence of the results obtained by ellipsometric and contact angle measurements for them. All silicon substrates for the samples were taken from a same silicon wafer cleaned as described in the experimental section. Ellipsometry measurement indicates that the thickness of the monolayer reached a plateau of 27Å, in reasonable agreement with the theoretical value (26Å) of complete monolayer,[36] after an exposure time of 1.5 hours. The advancing contact angle measurement suggests that a saturated value of 108° for the contact angle was reached at a lower exposure time (about 1 hour). This value is slightly lower than literature values of 111°-115°.[37] A much lower value of 98° of the advancing contact angle was reported by Dugger at al.[38] They used the almost same procedure as we used to form the SAMs. The difference of contact angle may be due to the different reaction conditions used, such as water adsorbed on the substrates,[18] and the structure of substrates.[20] It is believed that a thin SiO_2 film (approximately, 20Å in thickness) with a surface silanol (Si-OH) group concentration of ~$5x10^{14}$ cm^{-2} is obtained by Piranha etching.[39] The density of surface silanol groups on the native oxide is not enough for reacting of Si-Cl bonds with silanol groups. adsorbed water on the surface is needed to complete the reaction for forming fully-covered SAMs.[40,41] In addition, reaction temperature may also be a factor.[42]

To investigate quantitatively the surface coverage of SiC18 in the SAMs formed from solution with increasing exposure time, LFM imaging, XPS spectra, and FTIR spectra were conducted. The results are shown in Figure 2. It is obvious from the Figure that the growth behaviors

observed from the measurements of LFM, XPS and FTIR are consistent with one other, and with the thickness, contact angle measurements.

Friction signal depends on not only surface chemistry but also the load force used in LFM imaging.[43] A curve of friction *vs* load force was recorded firstly for the surface with fully covered SiC18 on silicon substrate, and a linear part in the curve was observed in the low load region up to ~70 nN. A mean load force of 40nN was chosen to measure the fiction signals. All the friction data reported here were taken using the same tip with the same load force, for meaningful quantitative comparisons. Friction signals from LFM imaging are showed in Figure2 (top). No surface damage was observed even after multiple scanning.

In Dugger's work,[38] the XPS spectra of Si 2p were consist of only two peaks at 98.5 eV due to Si, and 103 eV due to SiO_2. In terms of the relative constancy of SiO_2 component in the spectra with increasing exposure time, it was used as reference for quantification of OTS adsorption on silicon substrates. In our high resolution spectra, SiO_2 (2p) peak split. a small peak at ~101.7 eV was resolved by deconvolution. It may come from the SiO_2 at the most top on SiO_2 layer of the silicon substrates, which bond to the hydroxyl groups or the hydrocarbon chains of silane adsorbed onto the surface. The total intensity of the two components of SiO_2 (2p) spectra showed approximately constant for all the samples measured, which was used as the reference in our calculation. Only a single C 1s peak at 284.7 eV was observed consistent with basically only a single environment in the molecule, and the intensity of the peak increases with increasing exposure time. Using the ratio of C (1s) to SiO_2 (2p) signals shown in Figure 2 (middle), the relative concentration of SiC18 on surface can be determined.

A linear relationship between the amount of adsorbed OTS molecules and the $\nu(CH_2)$ absorption intensity in ATR spectra was reported in literature.[41] Silicon wafer is transparent for infra-red beam in the band of CH stretching vibrational modes. According to IR selective rules, CH stretching bands should be strong bands in transmission spectra, if the conformation of the silane molecules in the monolayers is that the hydrocarbon chains are approximately normal to the surfaces of the substrates. It is the case in our FTIR measurement, which supports the suggestion

that the incomplete monolayers form partially ordered islands rather than a spares homogeneous layer.[45] The absorbent spectra of FTIR transmission measurement, according to Beer's rule, is more reliable than reflection spectra of FTIR-ATR for quantification of surface coverage of SiC18 on silicon substrate. The total integrate intensity of $\nu_s(CH_2)$ and $\nu_{as}(CH_2)$ stretching modes was used to estimate the amount of SiC18 on the substrate as shown in Figure 2 (bottom).

In order to correlate friction force to surface coverage of SiC18 on substrates, the normalized relative friction forces between the surfaces covered with monolayer of SiC18 formed from solution and pure silicon wafer was calculated by the method as described in previous work.[34] The surface coverage of SiC18 was also estimated from the data of XPS and FTIR by normalizing the data respectively, with the data of saturated samples as normalized factors. The relationships between the normalized relative frictions of SAMs obtained from LFM images and surface coverage of SiC18 calculated by XPS and FTIR are summarized in Figure 3(top) and (bottom) respectively. Using these equations, we can semiquantitatively estimate the composition of SAMs from the value of the relative friction between the patterned areas and background areas as determined by LFM.

The traditional quantitative surface analytical technique, X-ray photoelectron Spectroscopy , has a mapping resolution in the order of 10μm.[46] Irradiation of the X-ray may also induce monolayer damage.[34, 47] Other microscopic imaging techniques such as SMIS are generally not capable of quantitative compositional mapping because of matrix effects.[48] FTIR observes an average information in a macroscopic area. The LFM technique in this work can be used for semiquantitative compositional mapping of patterned SAMs. Figure 4 shows the surface coverage of SiC18 in patterned areas obtained from friction measurement by LFM as a function of printing time. The inset is a LFM image of patterned SAM formed by microcontact printing for 2 minutes on silicon wafer with the 1mM solution of OTS in hexadecane as ink. The surface coverage of SiC18 in the patterned areas estimated by XPS, LFM and FTIR measurements are: 91%, 92% and 89% respectively. Both XPS and FTIR estimates are average results over a large measured area with a circle pattern of 20% on the surface as shown in the inset. The LFM result, however, is

directly deduced from the measurement of relative friction force between the patterned circle areas and background areas (pure silicon areas), which is a microscopic measurement. The FTIR signal of patterned sample was too weak to be very accurate due to only 10% cover of the patterned area on the sample surface (assuming that both sides of surfaces of the samples were derived with SAMs from solution). But the CH stretching bands were still observed. The coverage is also estimated from the two equations in Figure 3 by using LFM measurement. The same surface coverage of SiC18 of 95% in the patterned areas was obtained from the two equations for the pattern shown in the inset. No pattern of 100% surface coverage of SiC18 formed by μCP could be obtained even though the stamping time was increase to 3 minutes. It is more likely that formation mechanism of the SAMs from stamping and solution are different. The reactive site of the silane molecules became blocked when the monolayers were formed from the molecules inked on the surface of stamps to the substrates, while the molecules in solution were mobile to facility to form complete monolayers on substrates in enough time. Biebuyck et al [49] reported the order in microcontact printed SAMs of dodecanethiol on gold. More concentrate solution of the thiol was required by μCP than from solution to form SAMs indistinguishable from those formed from solution. Nano-scale defects in two-dimensional structure of the SAMs formed by μCP may be another reason.[50] Further effort will be put to understand the process of forming the monolayers by μCP and try to get the patterns with surface coverage of 100% SiC18.

LFM was used to image SAMs formed by OTS from solution. The surface frictions were also measured for the incomplete SAMs formed in different exposure time. The relative friction between the SAMs and pure silicon substrate correlated with the surface coverage of SiC18 in the SAMs. A correlation between the relative friction of the incomplete monolayers and the surface coverage of SiC18 in the incomplete monolayers was developed from LFM together with XPS and FTIR measurements. The surface coverage of SiC18 in patterned areas prepared by microcontact printing was estimated by using the correlation from relative friction between pattern areas and background locally measured by LFM. It demonstrates the feasibility and sensitivity of using LFM as an

alternative tools for locally quantitative analysis of surfaces and compositional mapping of μCP patterned, well-defined surface at the micrometer and perhaps at the submicrometer level.

References

1. Hopfiled, J. J.; Onnchic, J. N.; Beratran, D. N.; *Science* **1988**, *241,* 817.

2. de Gennes, P.-G. *Rev. Mod. Phys*, **1985**, *57*, 728.

3. Andle, J.; Vetelino, J.; Lec, R.; McAllister, D. *Proc. IEEE Ultrasonics Symp.* **1989**, 579.

4. Prime, K. L.; Whitesides, G. M. *Science* **1991**, *252,* 1164.

5. Linde, H,; Gleason, R. T.; *J. Polym. Sci., Polym. Chem.* Ed. **1984**, *22*, 3043.

6. Plueddemann, E. P. *J. Adhes.* **1970,** *2*, 181.

7. Xia, Y,; Mrksick, M.; Kim, E.; Whitesides, G. M. *J. Am. Chem. Soc.* **1995**, *117*, 9576.

8. Kumar, A.; Whitesides, H. A. *Appl. Phys. Lett.* **1993**, *63*, 2002.

9. Lea, A. S.; Pungor, A.; Hlady, V.; Andrade, J. D.; Herron, J. N.; Voss, E. W. Jr. *Langmuir* **1992**, *8*, 68.

10. Kumar, A.; Whitesides, G. M. *Science* **1994**, *236*, 60.

11. Singhvi, R.; Kumar, A.; Lopez, G. P.; Stephanopouos, G. N.; Wang, D. I. C.; Whitesides, G. M. Ingber, D. E. *Science* **1994**, *264*, 696.

12. Huang, Z.; Wang, P-C.; MacDiarmid, A. G.; Xia, Y.; Whitesides, G. M. *Langmuir* **1997**, *13,* 6480.

13. Lopez, G. P.; Biebuyck, H. A.; Harte, P.; Kumar, A.; Whitesides, G. M. *J. Am. Chem. Soc.* **1993**, *115*, 10774.

14. Lopez, G. P.; Biebuyck, H. A.; Whitesides, G. M. *Langmuir* **1993**, *9*, 1513.

15. Frisbie, C. D.; Martin, J. R.; Duff, R. R. J.; Wrighton, M. S. *J. Am. Chem. Soc.* **1992**, *114*, 7142.

16. Lopez, G. P.; Biebuyck, H. A.; Whitesides, G. M. *Science* **1993**, *260*, 647.

17. Hoffmann, H.; Mayer, U.; Krischanitz, A. *Langmuir* 1995, *11*, 1304.

18. Flinn, D. H.; Guzonas, D. A.; Yoon, R-H. *Collids Surf.* A **1994**, *87,* 163

19. Zasadzinski, J. A.; Viswanathan, P.; Schmartz, D. K.; Garnaes, J.; Madsen, L.; Chiruvolu, S.; Woodward, J. T.; Longo, M. L. *Collids surf.* **1994**, *93*, 305.

20. Peach, S.; Polak, R. D.; Franck, C. *Langmuir* **1996**, *12*, 6053.

21. Wilbur, J. L.; Biebuyck, H. A.; MacDonald, J. C.; Whitesides, G. M. *Langmuir* **1995**, *11*, 827

22. Bar, G.; Rubin, S.; Parikh, A. N.; Swanson, B. I.; Zawodzinski, T. A.; Whangbo, M. H. *Langmuir* **1997**, *13*, 373.

23. Bar, G.; Rubin, S.; Taylor, T. N.; Swanson, B. I.; Zawodzinski, T. A.; Chow, J. T.; Ferraris, J. P. *J. Vac. Sci. Technol. A* **1996**, *14*, 1794.

24. Hayes, W. A.; Kim, H.; Yue, X.; Perry, S. S.; Shannon, C. *Langmuir* **1997**, *13*, 2511.

25. Green, J.-B. D.; McDermott, M. T.; Porter, M. D.; Siperko, L. M. *J. Phys. Chem.* **1995**, *99*, 10960.

26. Tsukruk, V. V.; Reneker, D. H. *Polymer* **1995**, *36*, 1791.

27. Liu, Y.; Wu, T.; Evans, D. F. *Langmuir* **1994**, *10*, 2241.

28. Liu, Y.; Evans, D. F.; Song, Q.; Grainger, D. W. *Langmuir* **1996**, *12*, 1235.

29. Ohno, H.; Motomatzu, M.; Mizutani, W.; Tokumato, H. *Jpn. J. Appl. Phys.* **1995**, *34*, 1381.

30. McDermott, M. T.; Green, J.-B. D.; Porter, M. D. *Langmuir* **1997**, *13*, 2504.

31. Sarid, D. *Atomic Force Microscopy*; Oxford University Press: Oxford, 1991.

32. Huang, J,Y.; Song, K. J.; Lagoutchev, A.; Yang, P. k.; Chuang, T. J. *Langmuir* **1997**, *13*, 58.

33. Bhatia, S. K.; Teixeira, J. L.; Anderson, M.; Shiverlake, L. C.; Calvert, J. M.; Georger, J. H.; Hickman, J. J.; Dilcey, D. S.; Shoen, P. E.; Ligler, F. S. *Anal. Biochem.* **1993**, *208*, 197.

34. Zhou, Y.; Fan, H.; Fong, T.; Lopez, G., P. *Langmuir* **1998**, *14*, 660.

35. Wagner, C. D.; Riggs, W. M.; Davis, L. E.; Moulder, J. F.; Miutenberg, G E. *Handbook of X-ray Photoelectron Spectroscopy*; perkin-Elmer: Edern Praire, MN, 1979.

36. Ulman, A. *Ultrathin Organic Films*; Academic Press; San Diego, CA, 1991.

37. Cohen, S. R.; Naaman, R.; Sagiv, J. *J. Phys. Chem.* **1980**, *90*, 3054.

38. Rye, R. R,; Nelson, G. C.; Dugger, M. T. *Langmuir*, **1997**, *13*, 2965.

39. Ulman, A. *Adv. Mater.* **1990**, *2*, 573.

40. van Roosmalen, V. J.; Mol, J. C. *J. Phys. Chem.* **1979**, *83*, 2485.

41. Wasserman, S. R.; Whitesides, G. M.; Tidswell, I. M.; Ocko, B. M.; Pershan, P. S.; Axe, J. D. *J. Am. Chem. Soc.* **1989**, *111*, 5852.

42. Parikh, A. N.; Allara, D. L.; Azouz, I. B.; Roudelez, F. *J. Phys. Chem.* **1994**, *98*, 9577

43. Xiao, X.; Hu, J.; Charych, D. H.; and Salmeron, M., *Langmurir* **1996**, *12*, 235.

44. Banga, R.; Yawood, J.; Morgan, A. M.; Evans, B.; Kells, J. *Langmuir* **1995**, *11*, 4393.

45. Bierbaum, K.; Grunze, M. *Langmuir* **1995**, *11*, 2143.

46. Sherwood, P. M. A. In *The Handbook of Surface Imaging and Visulization*; Hubbard, A.T., Eds.; CRC Press: Boca Raton, 1995; p877.

47. Frydman, E.; Cohen, H.; Maoz, R.; Sagiv, J. *Langmuir* **1997**, *13*, 5089.

48. Tarlov, M. J.; Newman, J. G. *Langmuir* **1992**, *8*, 1398.

49. Larsen, N. B.; Biebuyck, H.; Delarmarche, E.; Michel, B. *J. Am. Chem. Soc.* **1997**, *119*, 3017.

50. Kumar, A.; Abbott, N. L.; Kim, E.; Biebyck,H. A.; Whitesides, G. M. *Acc. Chem. Res.* **1995**, *28*, 219.

Figure Captions

Fig. 1 Thickness of the SAMs formed from OTS measured by ellipsometry (top), and advancing contact angles of water (bottom) as the functions of exposure time of Si/SiO_2 substrates in solution (1mM OTS in hexadecane). All the substrates were cut from the same silicon wafer cleaned as described in text. The two sets of samples for each type of measurement were treated and analyzed concurrently.

Fig. 2 Friction signal of surface obtained from LFM imaging (top), C to SiO_2 ratio from XPS spectra (middle) and FTIR relative intensity (bottom), as the functions of exposure time. All the substrates were cut from the same Si wafer as the ones used for measurements of thickness and contact angle in Figure 1 and cleaned by Piranha. All the three sets of samples were treated concurrently with the sets used in Figure 1. C 1s and SiO_2 2p spectra were chosen to calculate the ratio of XPS in (middle). The $\nu(CH_2)$ stretching bands were chosen to get the integrated intensities (bottom).

Fig. 3 Normalized relative friction relative to pure silicon wafer as a function of surface coverage of SiC18 on substrates obtained from XPS spectra (top) and by FTIR (bottom). The coverage from XPS was calculated as the ratio of C 1s to SiO_2 2p signals of XPS spectra and the normalized factor was the C/SiO_2 ratio of the fully covered SAMs of SiC18. The coverage from FTIR was calculated by using the integrated intensity of $\nu(CH_2)$ stretching bands, and using saturated SiC18 monolayer as the normalized factor.

Fig. 4 Surface coverage of SiC18 in microcontact printed areas obtained from relative friction measurement by LFM as a function of patterning time. All of the samples were formed by patterning SAMs of SiC18 on substrates cut from the same Silicon wafer treated by Piranha, but with different stamping time. Inset is a LFM image of a sample patterned for 2 minutes. The dark

circle areas with lower friction are formed by OTS. The diameters of the circles are 5μm, and the distances between centers of circles are 10μm. Therefore the area of circles is ~20% of the whole substrate. The relative friction between the regions of circles and background is 0.056V, from which a surface coverage of 92% SiC18 in the patterned regions was estimated. XPS and FTIR measurements gave coverage of 91% and 89% for the patterned sample respectively. A coverage of 95% for the patterned areas was estimated from the two equations given in Fig. 3.

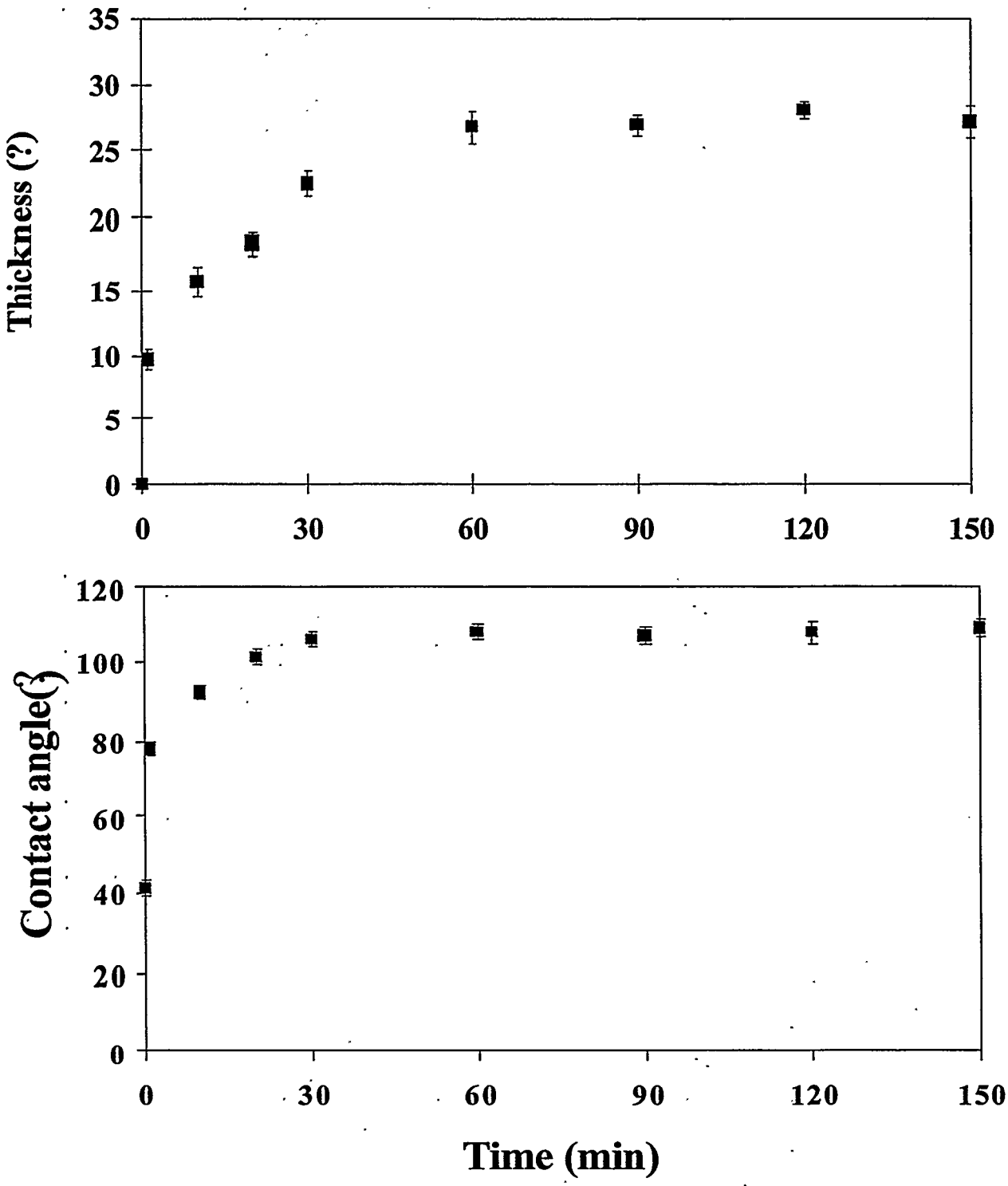
Thickness (?)
35
30
25
20
15
10
5
0
0
30
60
90
120
150
Contact angle(?)
120
100
80
60
40
20
0
0
30
60
90
120
150
Time (min)

Fig. (1)

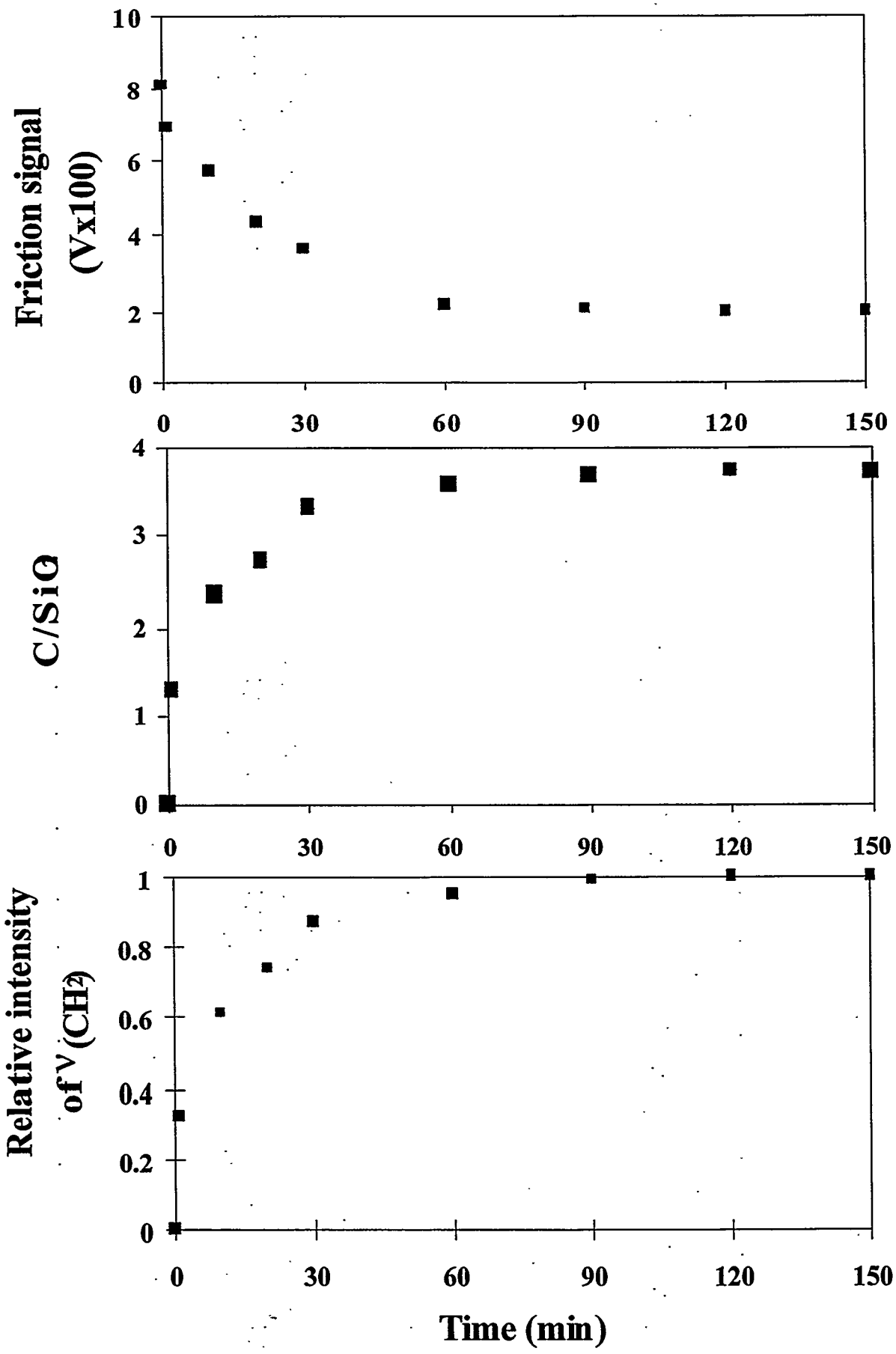
Friction signal (Vx100)
10
8
6
4
2
0
0
30
60
90
120
150
C/SiO
4
3
2
1
0
0
30
60
90
120
150
Relative intensity of ν(CH2)
1
0.8
0.6
0.4
0.2
0
0
30
60
90
120
150
Time (min)

Fig.(2)

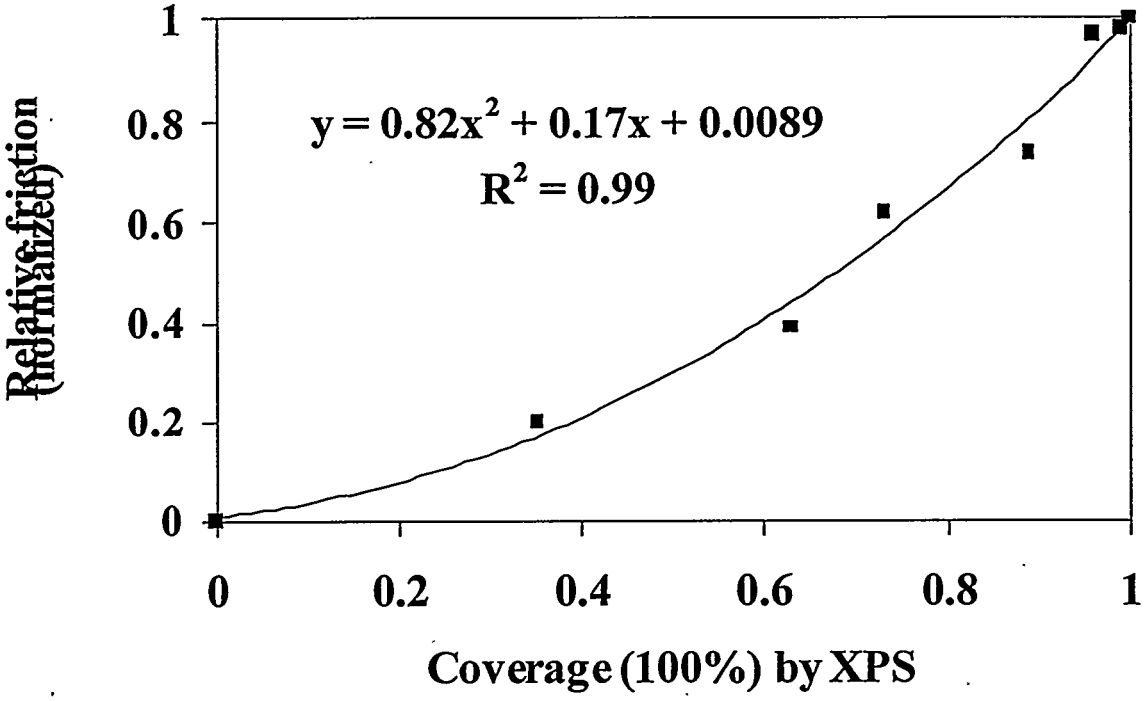
Relative friction (normalized)
y = 0.82x² + 0.17x + 0.0089
R² = 0.99
0
0.2
0.4
0.6
0.8
1
Coverage (100%) by XPS

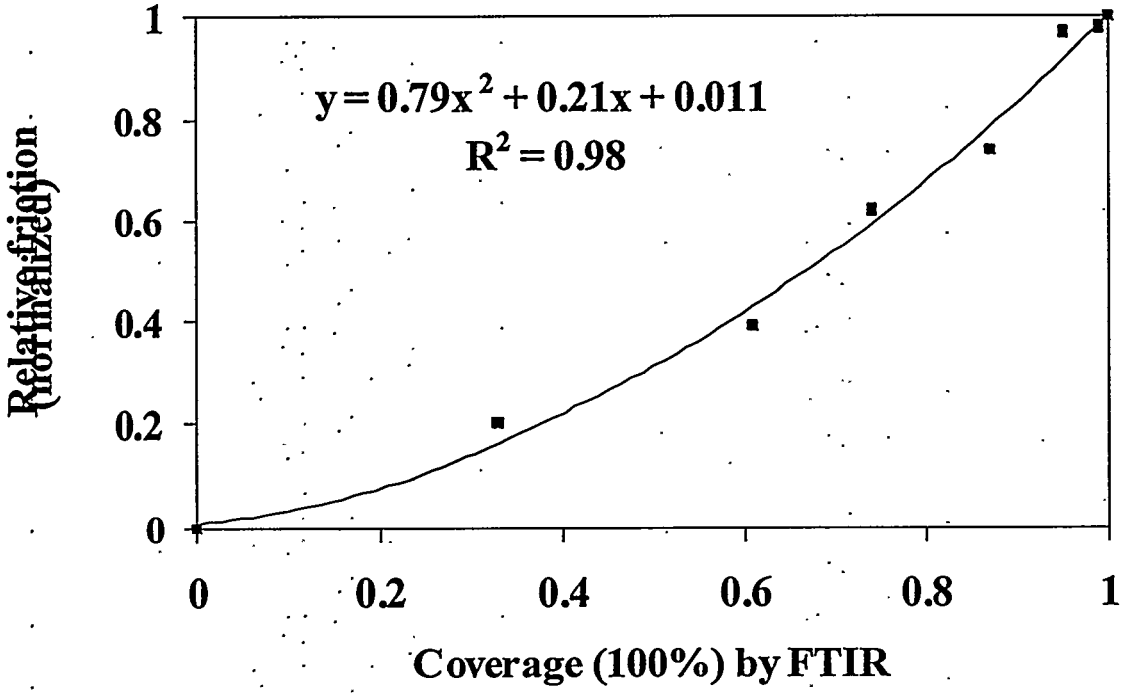
Relative friction (normalized)
y = 0.79x² + 0.21x + 0.011
R² = 0.98
0
0.2
0.4
0.6
0.8
1
Coverage (100%) by FTIR

Fig. (3)

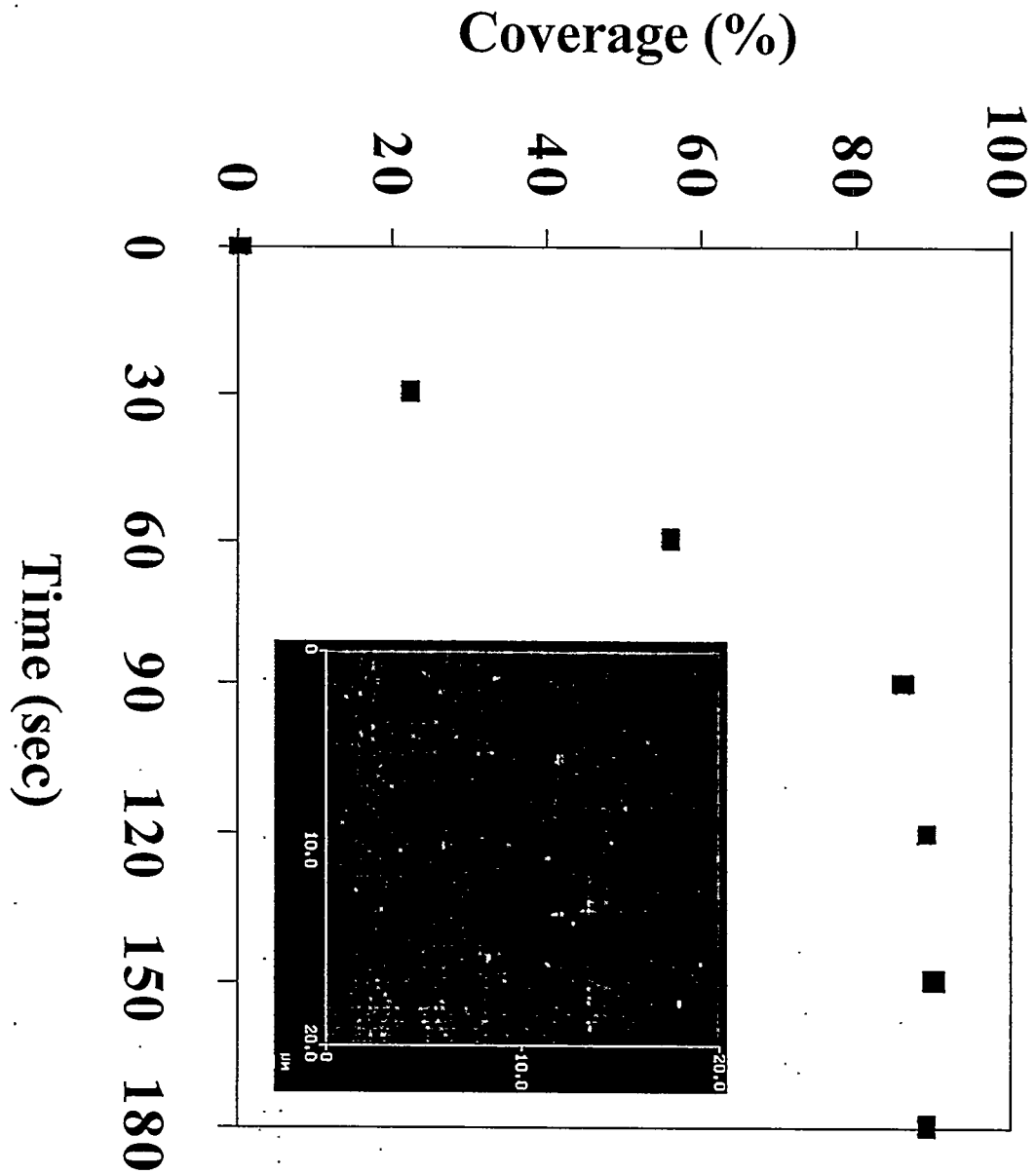
Coverage (%)
0
20
40
60
80
100
Time (sec)
0
30
60
90
120
150
180
0
10.0
20.0
0
10.0
20.0
μm

Fig. (4)

5. Surface treatment of micromachines (Sniegowski)

The root cause to the "silicon-wrap" residue, which potentially had precluded repeatable deposition of molecular lubricants to MEMS devices, was identified and eliminated. The root cause was identified as a silicon-rich initiation phase in the deposition of one of the sacrificial silicon dioxide films critical to the fabrication technology. A similar film did not occur on UC-Berkeley parts because they use a different deposition system for a comparable sacrificial oxide film. This is because they do not have the level of complexity available from their fabrication process as with the Sandia SUMMiT process, and therefore they do not require the specific type of silicon oxide deposition tool that is required in the SUMMiT technology. Specifically, we require a plasma-enhanced chemical vapor deposition (PECVD) system to properly backfill high-aspect ratio gaps defined in the polysilicon layers in preparation for subsequent planarization by chemical mechanical polishing. This sequence allows multi-layers of polysilicon, not available in the UC-Berkeley technology. In the warm-up and initiation steps of the PECVD oxide deposition, the film being deposited was slightly silicon-rich. Thus, the final release etch in hydrofluoric acid,, used to removed the oxide films, would only remove the "oxide" portion of the film leaving behind a porous, thin film of silicon (usually ~100Å, but thicker on occasion), i.e., the "silicon-wrap". This film could be removed by a 1:1:6 H_2O:H_2O_2:NH_4OH wet chemistry at high temperature. This was not the desired solution however.

Rather, the PECVD film deposition recipe was modified to include additional oxygen during the depostition, which effectively removed the initial silicon-rich phase. This solution provides very clean, released micromachine parts without any of the previous residue films suspect as potential interference in the subsequent deposition of molecular lubricants. This PECVD deposition recipe is now part of the baseline SUMMiT process.

6. Peformance of silane-lubricated micromachines (Miller)

The objective was to assess the impact of molecular scale lubricants on the performance of MEMS devices, with a particular emphasis on how the chemistry of the lubricants impacts performance. To achieve this objective, several MEMS devices were selected to provide the needed performance information. The first was a novel friction measurement device consisting of a flat horizontal beam that moves laterally against a round vertical post. A second device was the microengine, the primary power source driving virtually all of Sandia's actuated systems. Cantilever beams were also used to evaluate certain properties of the molecular scale lubricants prior to operational wear experiments.

While operational, measurement, and analysis methods for individual microengines had been previously developed, methods to achieve statistical performance data from many microengines were implemented this year. Results indicated that microengines generally wear out and fail with log-normal probability distributions. In addition, initial data were obtained on the specialized aforementioned friction structure to validate its usefulness for friction and wear studies. The intent was to then use these methods to evaluate various lubricant chemistries.

Very preliminary results obtained from the friction structures suggest that FDTS coatings provide a steady-state friction coefficient of approximately 0.02, nearly a factor of 7 less than ODTS. Friction device lifetimes for FDTS and ODTS coatings were not markedly different, but did appear to be better by nearly a factor of 4 than uncoated (supercritically dried only) samples.

Subsequent experiments indicated that the molecular scale lubricant application process exhibited considerable variation and was not well controlled. In particular, free beam length (an indicator of the adhesion energy) varied dramatically for process runs that were intended to be identical. Microengine lifetimes did not correlate with free beam length, suggesting that either the lubricants did not coat the rubbing surfaces or the lifetime was governed by properties other than those of the molecular scale lubricant. There was certainly evidence of the latter; as microengines were operated to failure, wear of the rubbing surfaces abraded away material many orders of

magnitude thicker than the presumed thickness of the monolayer coatings. Any benefit of the lubricant would certainly have been lost early in the life of the engine.

Conclusions regarding how the chemistry of the lubricants (e.g. chain length) impact performance could not be drawn because of the lack of reproducibility of the coating process.

DISTRIBUTION

3	MS1413	A. R. Burns, 1114
1	MS1413	T. A. Michalske, 1114
1	MS1413	J. E. Houston, 1114
1	MS1413	T. M. Mayer, 1114
1	MS1080	J. J. Sniegowski, 1725
1	MS1080	S. L. Miller, 1725
1	MS0340	M. T. Dugger, 1832
1	MS1111	M. J. Stevens, 9225
2	MS0188	LDRD Office, 4001
1	MS9018	Central Technical Files, 8940-2
2	MS0899	Technical Library, 4916
1	MS0619	Review & Approval Desk, 15102 For DOE/OSTI